Polytechnic of Leiria
School of Technology and Management
Department of Electrical and Electronics Engineering
Master's in electrical and electronic engineering – Electronics and telecommunications

DESIGN AND TEST OF RF SHIELDING FOR BEAM IMPEDANCE REDUCTION IN CERN ACCELERATORS

MIGUEL VALENTE DOS SANTOS

Leiria, September of 2023

This page is intentionally left blank.

Polytechnic of Leiria
School of Technology and Management
Department of Electrical and Electronics Engineering
Master's in electrical and electronic engineering – Electronics and telecommunications

DESIGN AND TEST OF RF SHIELDING FOR BEAM IMPEDANCE REDUCTION IN CERN ACCELERATORS

MIGUEL VALENTE DOS SANTOS
Number: 2182460

Internship supervised by Professor Telmo Rui Carvalhinho Cunha Fernandes (telmo.fernandes@ipleiria.pt) and Christine Vollinger (Christine.Vollinger@cern.ch).

Leiria, September of 2023

This page is intentionally left blank.

ACKNOWLEDGMENTS

Firstly I would like to express my deepest gratitude to Dr. Christine Völlinger, form CERN, for offering me this unique internship opportunity. Christine played a pivotal role in shaping my understanding of RF measurements and provided me with invaluable training that laid the foundation for this work. I am also grateful for the countless hours she invested in patiently explaining complex concepts and techniques. She was always very kind and supportive, I am truly fortunate to have had her as my supervisor.

I want to thank Professor Telmo Fernandes for his teachings, continuous supervision and guidance at ESTG over the past years. He always had a word of encouragement during moments of uncertainty.

Thank you to all my colleagues from RF-BR section for creating an awesome work environment, all the lunch talks and much needed coffee-breaks. A very special thanks goes to Michela Neroni and Michael Sullivan for their invaluable help during measurements and all the discussions related to CST simulations.

Thanks to my friends Ze and Guilherme that despite being far away, they were always close.

Last but not least, I am profoundly grateful to my loving wife Maria, my parents and brother. Their love, understanding, and encouragement have been my pillar of strength during this journey.

This page is intentionally left blank.

RESUMO

O CERN, Organização Europeia para a Pesquisa Nuclear, é um dos maiores laboratórios do mundo dedicado à física de partículas de alta energia. No CERN, aceleradores de partículas e detetores são utilizados para estudar os constituintes básicos da matéria. O acelerador principal do CERN é o *Large Hadron Collider* (LHC), o acelerador de partículas mais poderoso construído até ao momento. No entanto, ele não funcionaria sem a sua cadeia de injetores de aceleradores. Esta cadeia começa com o LINAC4, seguido pelo PSB, PS e SPS, que injeta as partículas no LHC.

Aceleradores de partículas relativamente recentes, como o LHC, foram projetados desde o início para terem a *beam coupling impedance* mais baixa possivel. No entanto, o mesmo não se aplicou aos aceleradores mais antigos do CERN, projetados e construídos há décadas, originalmente destinados a intensidades de feixe muito menores. Atualmente, um dos fatores limitantes para aumentar as intensidades do feixe são as instabilidades causadas pela *beam coupling impedance* dos aceleradores mais antigos na cadeia, como o PS.

Os coletores de vácuo do PS foram identificados como uma fonte de instabilidades devido terem uma alta impedância. A contribuição atual de impedância desses coletores foi simulada e medida. Várias possíveis soluções de blindagem, com o objetivo de reduzir a impedância, foram estudadas e simuladas, obtendo resultados promissores.

Medições rotineiras de outros componentes do acelerador foram realizadas, seja para completar a base de dados da *beam coupling impedance* do acelerador ou para avaliar se a blindagem instalada é eficaz. Numa dessas medições, foi constatado que um *Septa magnet* sobressalente do PS apresentava *RF fingers* defeituosos, e a blindagem não era eficaz.

Keywords: Simulação eletromagnética, Aceleradores de partículas, *Beam coupling impedance*, Medições RF.

This page is intentionally left blank.

ABSTRACT

CERN, the European Organization for Nuclear Research, is one of the world's largest laboratories for high-energy particle physics. At CERN, particle accelerators and detectors are used to study the basic constituents of matter. CERN's flagship accelerator is the Large Hadron Collider (LHC), the most powerful particle accelerator built up to now. However, it would not work without its accelerator injector chain. This chain starts with LINAC4, followed by PSB, PS, and SPS, which inject into the LHC.

Relatively new particle accelerators like the LHC were designed from scratch with a limited overall beam coupling impedance budget in mind, but this was not the case for the older accelerators at CERN, designed and built decades ago and originally intended for much lower beam intensities. Currently, one of the limiting factors to increase the beam intensities is instabilities caused by the beam coupling impedance of the older accelerators in the chain, such as the PS.

The PS vacuum manifolds were identified as one source of instabilities due to a high beam coupling impedance. The current impedance contribution of the manifolds was simulated and measured. Several possible shielding solutions, aimed at reducing the beam coupling impedance, were studied and simulated, giving promising results.

Routine RF measurements of other components of the accelerator were performed, either to complete the accelerator impedance contribution database or to assess whether or not the installed shielding is effective. During one of these measurements, it was found that a spare PS septa magnet had defective RF fingers, and the shielding was not effective.

Keywords: Electromagnetic simulation, Particle accelerators, Beam coupling impedance, RF measurements.

This page is intentionally left blank.

TABLE OF CONTENTS

LIST OF FIGURES

This page is intentionally left blank.

LIST OF TABLES

This page is intentionally left blank.

LIST OF ACRONYMS

BLonD	Beam Longitudinal Dynamics code.
BPM	Beam position monitor.
CERN	European Organisation for Nuclear Research.
CODD	Closed orbit digital display.
CST	Microwave and Particle Studio suite of Computer Simulation Technology company.
DUT	Device under test.
EM	electromagnetic.
FEM	finite-element method.
LHC	Large Hadron Collider.
LINAC	linear accelerator.
LIU	LHC injectors upgrade.
PS	Proton Synchrotron.
PSB	Proton Synchrotron Booster.
RF	Radio-Frequency.
SPS	Super Proton Synchrotron.
VNA	Vector Network Analyser.

This page is intentionally left blank.

1

INTRODUCTION

1.1 THE CERN ACCELERATOR COMPLEX

CERN, the European Organization for Nuclear Research, is one of the world's largest laboratories for high-energy particle physics. At CERN, particle accelerators and detectors are used to study the basic constituents of matter. Since its foundation in 1954, physicists and engineers have unified their efforts towards increasing the discovery potential and pushing the limits of the energy frontier of the accelerators. To this purpose, CERN hosts a complex of machines that accelerates protons or ions to almost the speed of light and delivers them to various experiments such as fixed-target experiments or the detectors of the Large Hadron Collider (LHC) [2].

The flagship accelerator of CERN is the LHC, world famous for being the most powerful particle accelerator built up to now. LHC, however, would not work without its accelerator injector chain starting with the linear accelerator LINAC4, where particles are accelerated to 160 MeV before they pass to the Proton Synchrotron Booster (PSB), where their kinetic energy is pushed to 2 GeV. Next, they are injected into the Proton Synchrotron (PS) from where they are transferred to the Super Proton Synchrotron (SPS) and then to the Large Hadron Collider (LHC). In the LHC, the highest energy that a particle could reach is currently 6.8 TeV when the particles are brought to collision in one of the four experimental points called Compact Muon Solenoid (CMS), A Large Ion Collider Experiment (ALICE), Large Hadron Collider beauty (LHCb) and A Toroidal LHC ApparatuS (ATLAS). The CERN accelerator complex is depicted in Fig. 1.

In general, two types of accelerators are distinguished by their shape, circular and linear, and both have their benefits and their drawbacks. To be more specific, linear accelerators mainly consist of accelerating cavities, and each particle is passing the accelerating structure only once. Thus, the maximum energy achievable in a linear accelerator is limited by its length. On the other hand, circular accelerators make repeated use of the installed accelerating cavities as the particles can pass the same structure again and again. The highest achievable energy of circular accelerators is nowadays limited by the magnetic field strength of superconducting dipole magnets required to keep the particles on their circular trajectory.

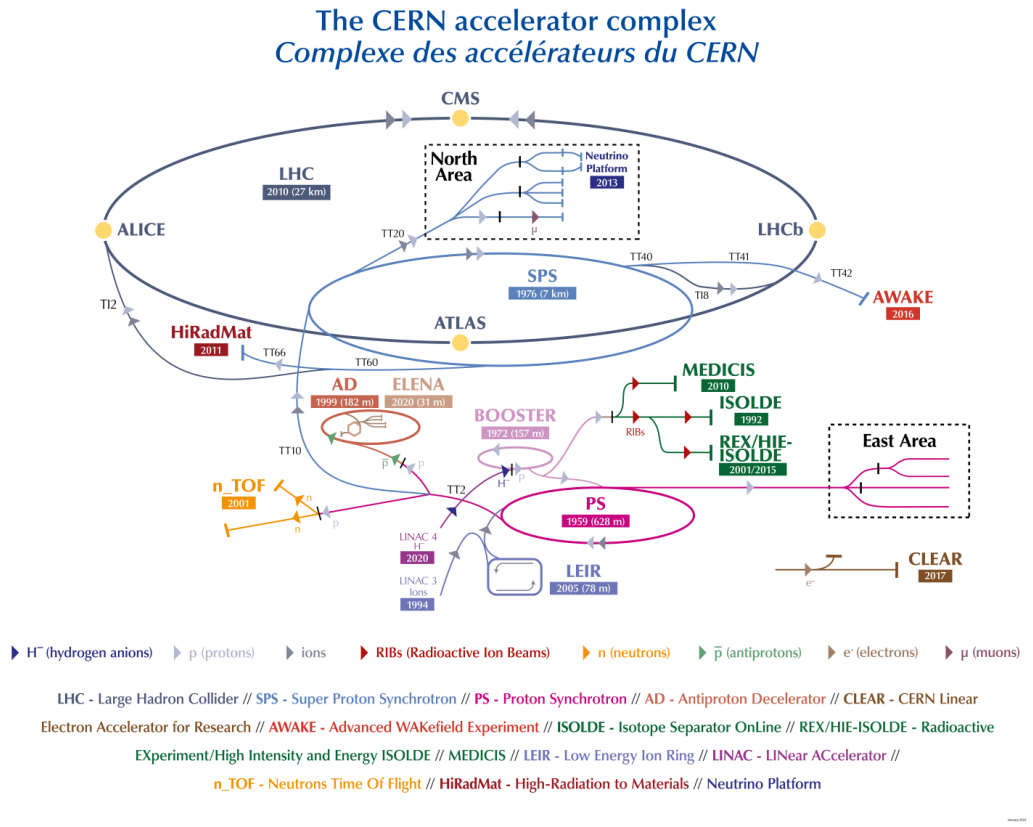

Figure 1: Illustration of CERN accelerator complex. © CERN

1.2 THE CONCEPT OF BEAM COUPLING IMPEDANCES

In particle accelerators, a package of particles, so-called bunches, are accelerated instead of single particles. The word "beam" refers to the assembly of all bunches in the accelerator.

The part of a particle accelerator that is closest to the beam and therefore creates the most interaction, is the vacuum chamber. Ideally, this vacuum chamber would be a smooth pipe to keep this interaction with the beam to a minimum. In the real accelerator, however, the beam vacuum pipe is composed by several components that interrupt its ideal uniform cross-section. These elements are, for example, the beam pipe itself when it changes its size to provide sufficient aperture for the beam, mechanical expansion bellows, connection flanges, vacuum pumping ports, including so-called pumping manifolds, etc. In addition, the beam pipe is interrupted by different machine elements, such as accelerating RF cavities, beam instrumentation monitors, e.g., for measuring beam size or position, insertion and extraction kickers to get the beam in and out of the accelerator, scrapers to reduce the transverse beam size, septa to deflect the beam, and others. These components have different shapes/dimensions and may contain different materials, therefore such

a complexity constitutes an unavoidable non-uniformity of the beam surrounding structure throughout the entire accelerator.

The interaction of a bunch of charged particles when it passes though such a discontinuity (i.e. cross-sectional variation) in the beam pipe, generates electromagnetic (EM) fields at the location of the discontinuity that may propagate along the beam pipe and resonate in the different elements [15], e.g a pumping port or bellows. These EM fields are stronger or weaker depending if the transition/discontinuity is abrupt or only gradual. These EM fields may be trapped or propagate in the vacuum chamber, and in any case they will not only influence the exciting bunch itself, but depending on the decay time of the fields also impact on the following bunches. This is even more significant in the case of circular accelerators, in which the particles go through the same type of disturbance in every turn. Due to this interaction of the beam with the surrounding accelerator components, the beam quality can get degraded, leading to beam instabilities and potentially beam loss, in the worst case. Consequently, these instabilities impose a severe limitation to increasing the beam intensity.

Further important considerations are the effects of this beam-induced EM fields on the different machine elements. High intensity EM fields can excessively heat sensitive elements close to the beam, which will not only produce an undesirable increase in vacuum pressure, but also damage or even destroy these elements. The generation of EM fields by the beam also takes energy away from the beam, thus increasing the required power to be provided by the RF accelerating cavities. Particles which are lost from the beam due to induced EM fields may hit the walls of the vacuum chamber, damaging them and produce excessive radiation.

The strength of the interaction of the generated EM wake fields can be characterised by the beam coupling impedance which is defined as the integral over the normalised Fourier transform of the EM force along the particle trajectory. The beam coupling impedance (also referred simply as impedance) is described by three spatial components, the longitudinal, i.e. along the beam pipe, and transverse (in the planes horizontal and vertical to the propagation direction of the beam).

The impedance is a complex function. The real, i.e. resistive, part of the longitudinal impedance describes the energy loss, while the imaginary, i.e. reactive, part shifts the frequency of the beam oscillation.

The scope of this work is focused in the longitudinal component only, due to the fact that this is the component responsible for the beam instabilities in the PS machine.

For all the reasons mentioned before, it is very important to keep the beam coupling impedance as low as possible on all the elements that are part of the

vacuum chamber, either by taking this into consideration at the designing stage of the accelerator or by applying modifications to individual components in older accelerator parts.

1.3 MOTIVATION FOR THIS WORK

Relatively new particle accelerators like the LHC were designed from scratch with a limited overall beam coupling impedance budget in mind. This, however, was not the case for the older accelerators at CERN designed and built decades ago and originally intended for much lower beam intensities. Performance limitations arising from the injector chain with regard to the increased beam intensity were therefore addressed by the LHC injectors upgrade (LIU) project [6]. Within this project, each accelerator in the injector chain underwent extensive studies with the goal to increase the beam intensity and stability of the beam injected into the LHC. Several critical impedance sources of the CERN accelerator complex were identified and possible mitigation measures were studied. Within these impedance reduction campaigns, databases for all machines, consisting of their most relevant impedance contributors were created over the last years, both by bench measurements and full-wave EM field simulations of different accelerator devices. These databases provide the necessary input for macro-particle simulations which allow to study the dynamic behaviour of different beams and machine configurations in the respective accelerators.[4]

As is stated by its name, the PS machine (PS stands for proton synchrotron) is working with the synchrotron principle, i.e., it is a circular accelerator that synchronizes the frequency of the accelerating cavities with the bending field in the magnets. One of the components identified as a large contributor for the overall beam impedance of the PS accelerator, are its vacuum pumping ports (also known as vacuum manifolds). These vacuum manifolds are essentially a hollow tube installed transversely on the beam pipe leading to an asymmetric pumping structure. The pumping structure is carrying on one side an ultra high vacuum pump, on the other side, the manifold is equipped with a flange that allows a Beam Position Monitor (BPM) to be inserted in the beam line, as will be shown in detail in the next sections. Depending on whether a manifold is equipped with a BPM or not, its contribution to the beam impedance is different. Empty manifolds are currently unshielded and they act as an unwanted cavity and multiple EM fields are exited by the passing beam contributing to beam instabilities and thus limiting the maximum beam intensities that can be reached in the PS. There is one of these manifolds after each bending magnet, totaling to 100 manifolds. Out of these, 55 are fitted

with a beam instrumentation device, 8 have an additional pumping unit and the remaining 37 are empty i.e., only equipped with a simple flange cover.

1.4 REPORT OUTLINE

The present report is organized in 5 chapters. Chapter 1 introduces CERN and its accelerators, the concept of beam coupling impedance is explained and the motivation for this work is presented.

In Chapter 2, the impedance contribution from the vacuum manifolds is studied in the two most common configurations, the empty manifold an the manifold equipped with a beam instrumentation device. Simulation data and RF measurements are shown.

Chapter 3 presents possible mitigation methods to reduce the manifolds impedance. Several shielding solutions are simulated and compared.

In Chapter 4, the case of the PS spare fast extraction septum, the SMH16, is presented. Where routine RF measurements revealed a defect in the device internal RF shielding.

Finally, Chapter 5 presents some conclusions about the achieved results.

This page is intentionally left blank.

2

IMPEDANCE CONTRIBUTIONS IN THE PS MACHINE - VACUUM MANIFOLDS

The beam intensity levels required in LHC have been increasing over the years, and this required that all the accelerators in its injection chain to be able to keep up with these increase in their beam intensities. To accomplish this, several upgrades to the accelerators have been made over the past years, starting from the top of the chain, the SPS, followed by PS, PSB and LINAC4. The PS accelerator was originally designed and built, in the decade of 1950, for a much lower beam intensity than what it is required nowadays. The beam impedance of the parts originally designed was not a limiting factor at the time. One of the components identified as a significant contributor, for the overall beam impedance of the PS and thus limiting its performance, are the vacuum manifolds.

2.1 PROBLEM DESCRIPTION

The vacuum manifolds are assembled in the downstream position of every dipole magnet (bending magnets). Figure 2 shows the illustration of one complete magnet unit (including the manifold and ultra high vacuum pump). As already mentioned, the PS machine has in total 100 of these assemblies installed.

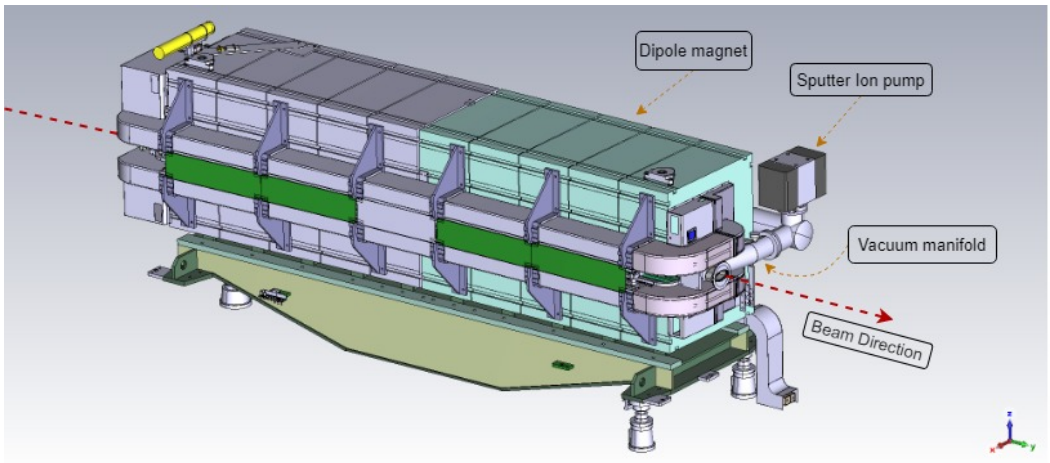

Figure 2: 3D drawing of a magnet unit assembly [11].

Figure 3 shows in more detail the vacuum manifold assembly. The manifolds are equipped with an ultra high vacuum pump installed on one side, and on the square

flange is possible to install other equipment like a BPM or an additional pumping unit. Of the total number of 100 of these flanges in the PS machine, 55 are equipped with a beam instrumentation device, 8 have an additional pumping unit, and the rest of them are empty having only a flange cover installed.

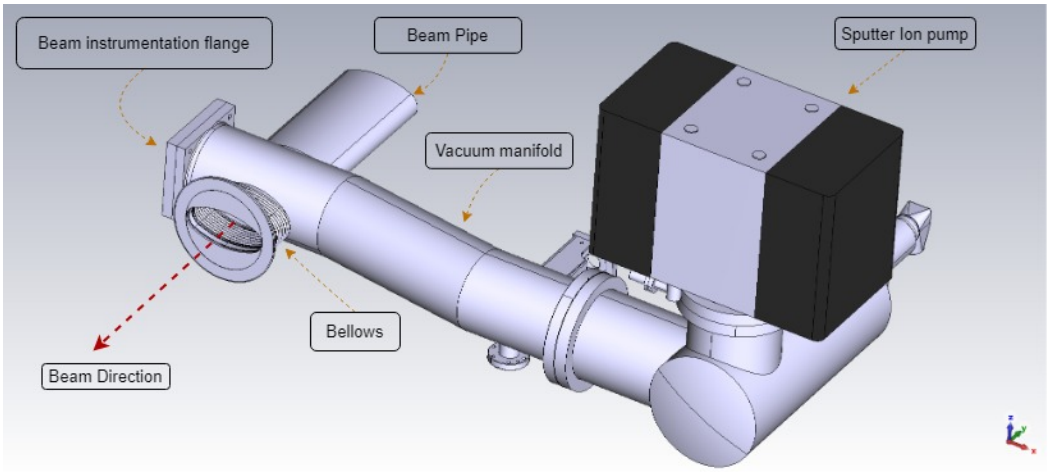

Figure 3: 3D drawing of a complete vacuum manifold assembly.

In general there are two ways to evaluate the impedance contribution of a given part of the accelerator, in this case the manifold: One way is by means of numerical simulations, using CST software [5]; the other one is by carrying out an RF-measurement on the device. Whenever possible or reasonable both ways are used, where the later is used to benchmark the results from the simulations.

2.1.1 *CST simulation of the vacuum manifolds*

As a first approach a CST Eigenmode and Wakefield simulations were performed.

Creating an impedance simulation model requires a 3D geometry of the part to be evaluated. Over the years CERN has put a lot of effort to create an extensive 3D drawing database of most of its accelerator parts, however, this database is complete only for newer accelerators. Consequently, this is not the case for older machines like the PS, where only 2D paper drawings are available for some of the parts. This effort of creating the 3D drawing was not done for older parts that are too complex and that are planned to be replaced by updated versions.

For the vacuum manifolds there is a 3D geometry available, and the first step after loading the file in CST is to simplify the geometry. This simplification is done by removing unnecessary detail in the geometry that has no influence on beam, for example everything that is outside of the vacuum tube/chamber like holes in flanges or the mechanical support structure. In addition, the structure close to the beam needs to be modified, i.e. the geometry details have to be simplified to allow

simulation with FEM solvers. This concerns for example, changing small chamfers or blends/fillets to sharp edges, remove or model screw heads as cylinders, model complex RF fingers as sharp solid, etc. Parts on the inside of the vacuum chamber have to be very carefully evaluated as to which details it is possible to remove or modify, to avoid that an oversimplification of the EM-calculation that may lead to a completely inaccurate result. This process is often called model order reduction and a graphical illustration of this can be seen in figure 4. For example, the modeling of a small chamfer of 1 mm in a part inside a cylindrical vacuum chamber with 80 cm of diameter and 1 m of length may require millions of additional mesh cells, which significantly increases the simulation time without having a significant impact on the results. Also, when importing to CST 3D geometries created using some other CAD software, it is often necessary to check if faces that are supposed to be touching each other are in fact truly contacting. It can happen that after importing the geometry to CST two given parts may appear to be touching but in reality there is a tiny gap of a fraction of a millimeter that is separating them. This has to be corrected as well, as it can fail to create the mesh, or lead to extensive meshing in the area that could even give completely wrong results. This is often the most crucial and time consuming step as such simplifications and corrections are needed in order to perform simulations within an acceptable amount of time, but at the same time with reliable and reproducible results.

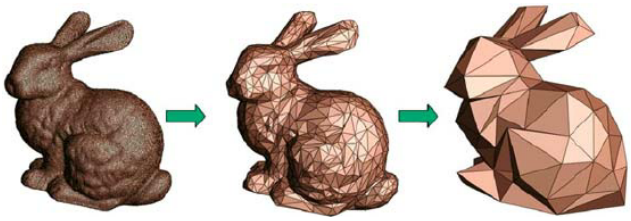

Figure 4: Graphical illustration of model order reduction [12]

After simplifications are performed, the CST Eigenmode or wakefield solver is selected, the path where the beam passes in the geometry is defined and the beam parameters are set. The three beam parameters are:

- Relativistic β: is used to define the velocity of the charged beam particles, it can be a value between 0 and 1, being 1 the speed of light.
- Particle charge: specifies the test charge of the particle bunch and is set to 1e-9 C.
- Standard deviation σ: Sigma defines the standard deviation of the gaussian bunch in length units, this parameter is used by the solver to define the stop frequency of the simulation (and mesh size). A sigma of 65 mm is used, which results in a simulation stop frequency of approximately 1.6 GHz.

The last step is filling the structure with vacuum and setting the boundaries as open in the beam axis and closed on the other surfaces.

2.2 EMPTY MANIFOLD

2.2.1 *CST Simulations*

Figure 5 shows the CST model for the vacuum manifold after performing the steps described before. This model is for the case where the manifold is empty, i.e. there is no beam instrumentation device inserted. Moreover the sputter ion pump and the big chamber section where it connects to (see Figure 2), do not need to be considered for simulation.

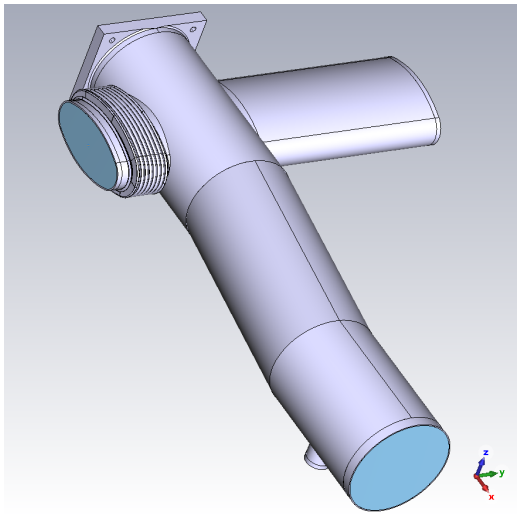

(a) Manifold CST model.

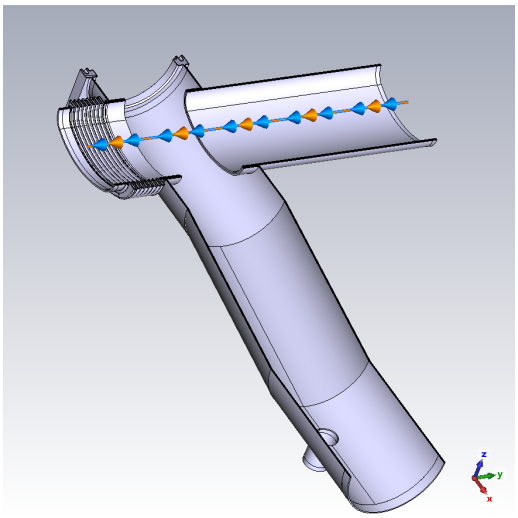

(b) Longitudinal cut with beam axis shown by the arrows.

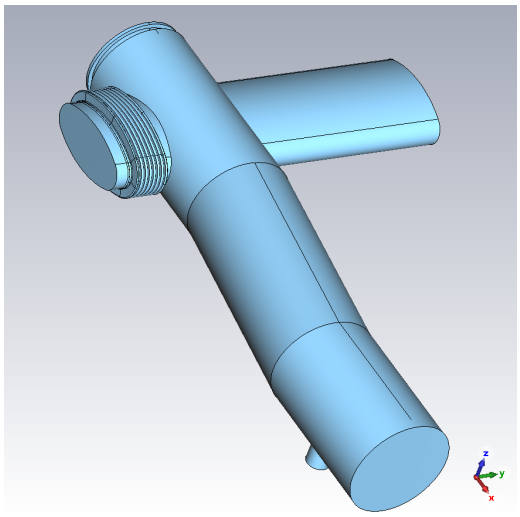

(c) Vacuum fill.

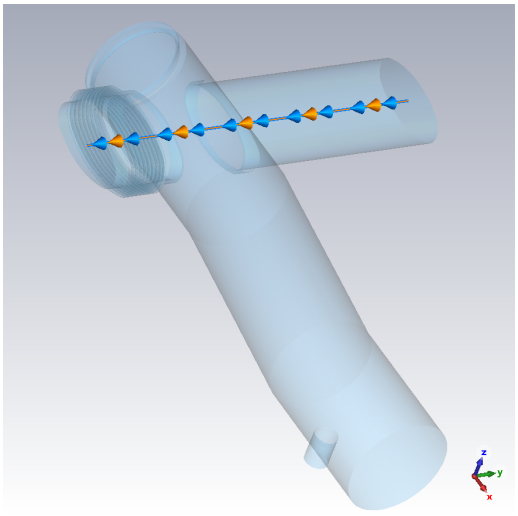

(d) Vacuum fill with beam axis shown by the arrows.

Figure 5: Vacuum manifold CST model.

In Figure 6 a plot of the computed wake impedance of the vacuum manifold is shown, were four strong resonance peaks located at 1219 MHz, 1264 MHz, 1338 MHz and 1426 MHz can be observed.

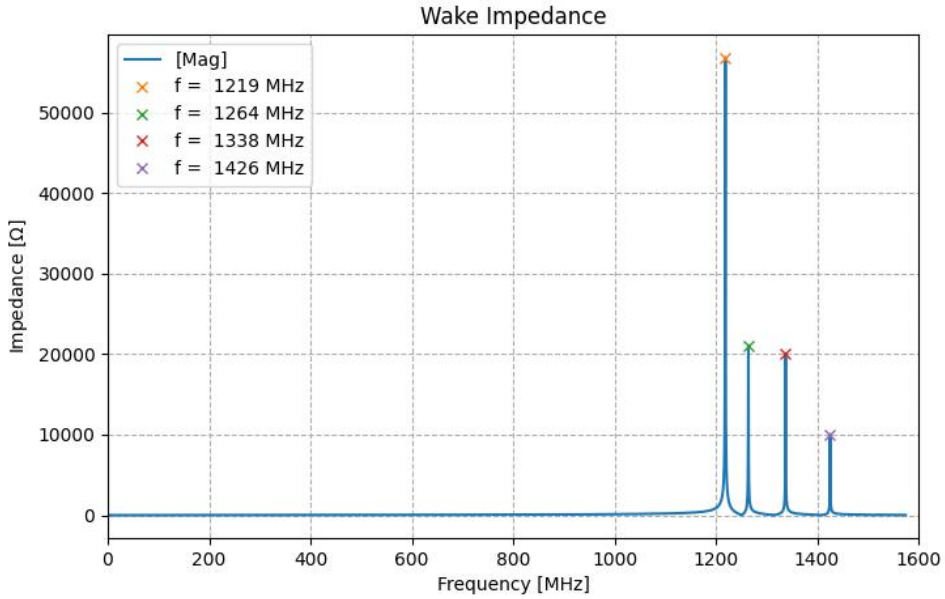

Figure 6: Empty manifold wakefield Impedance simulation result.

Figure 7 shows the electric field configuration for every resonant peak, inside of the vacuum manifold. In this case there is a big cross-section variation where the beam pipe connects to the manifold, this forces the image current (induced by the traveling bunch, in the beam pipe wall) to go through a longer path. This excites and traps various unwanted modes that resonate inside the chamber, as seen in figure 7, and possibly disturbing the following bunches.

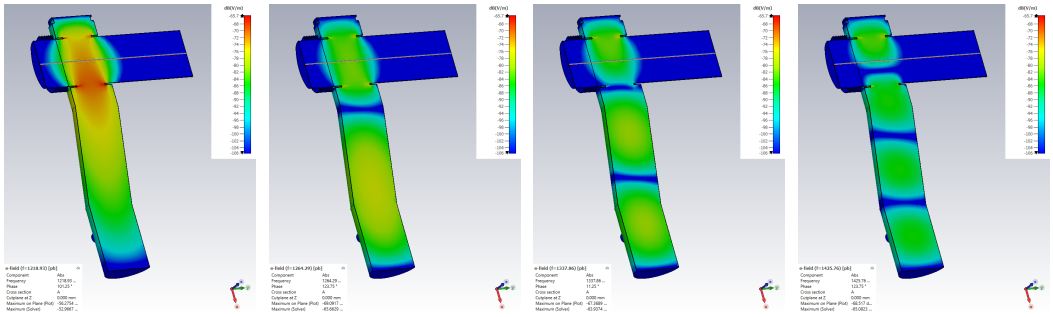

(a) 1219 MHz (b) 1264 MHZ (c) 1338 MHZ (d) 1426 MHZ

Figure 7: Electric field configuration of the four resonance peaks.

An eigenmode simulation was also performed to have a cross-check on the resonances calculated by the wake field simulation previously explained. The eigenmode simulation is used to calculate the frequencies and the corresponding electromagnetic field patterns (eigenmodes), of a given structure, when no excitation is applied. The

eigenmodes or resonant frequencies calculated by this solver are dependant on the the physical geometry and material properties of the given structure.

The setup process for this type of simulation follows the same steps as for the wakefield simulation, except the definition of a beam and its parameters. Instead, for this type of solver, the number of modes to be calculated have to be specified as well as the starting frequency. If the starting frequency is set to 0 it may be necessary to request the calculation of dozens or even hundreds of modes to get results for the entire frequency band of interest, this leads to a very long computation time and very large simulation files (dozens of GB). In this case, a wakefield simulation was performed first, so it is known that the resonant modes start to appear around 1.2 GHz. It is possible to take advantage of that and reducing simulation time by setting the start frequency for example at 900 MHz. It may be necessary to re-run the simulation several times and increase the number of modes to calculate, as in the beginning it's not known how many modes, and at which frequencies, the solver will detect.

The simulation will result in a list of the detected modes, and the 3D configuration of the electric and magnetic fields for each detected mode. This information alone is not of much use because the solver will detect all the modes that are possible to be excited in the given geometry, but that doesn't mean that the passing beam in the particle accelerator is able to excite all of them.

To make the distinction of what modes are relevant, further post-processing steps have to be taken. In CST it is possible to calculate, as post-processing, the so-called accelerator figures of merit for each of the modes, being them: the Shunt impedance (R_{shunt}), the Unloaded quality factor (Q_0) and the R-over-Q (R/Q) .

- Shunt impedance R_{shunt} is a measure to define the **effectiveness** of the cavity to provide a certain axial voltage for a defined power P. Shunt impedance is usually in the range of Mega ohms, as a design goal, the shunt impedance shall be as large as possible, as large voltage is desired. Note that the shunt impedance is independent of the cavities excitation level[14].
- Unloaded quality factor Q_0 is the well known characteristic value to express the resonating peak. High Q-values give a narrow peak of high quality. In general, the unloaded Q_0 is defined as the average energy stored in the resonator normalised to the -energy dissipated in the resonator (=power lost by dissipation on its walls), i.e., $Q_0 = \frac{\omega U}{P}$. In practice, the Q-factor is determined from the frequency reading of the so-called 3-dB-points and the resonant frequency. Note that due to the loading effect of the measurement connection, only loaded Q can be measured: $Q_L = \frac{f_{res}}{\Delta f}$.

- R-over-Q (also called R-upon-Q), measure of cavity acceleration **efficiency** at a given frequency $R/Q = \frac{(V_0 T)^2}{\omega U}$. Note that the ωU-term comes from the definition of the Q-value and that T is the so-called transit time factor that takes into account the time which is needed by the particle to pass through the cavity (and the fact that the cavity will not be on maximum voltage during this passage).

The plot of figure 8 shows the R/Q values from the eigenmode simulation overlaid with the results from the wake field simulation. The results from the two types of simulation show good agreement and the detected peaks differ only in a few MHz.

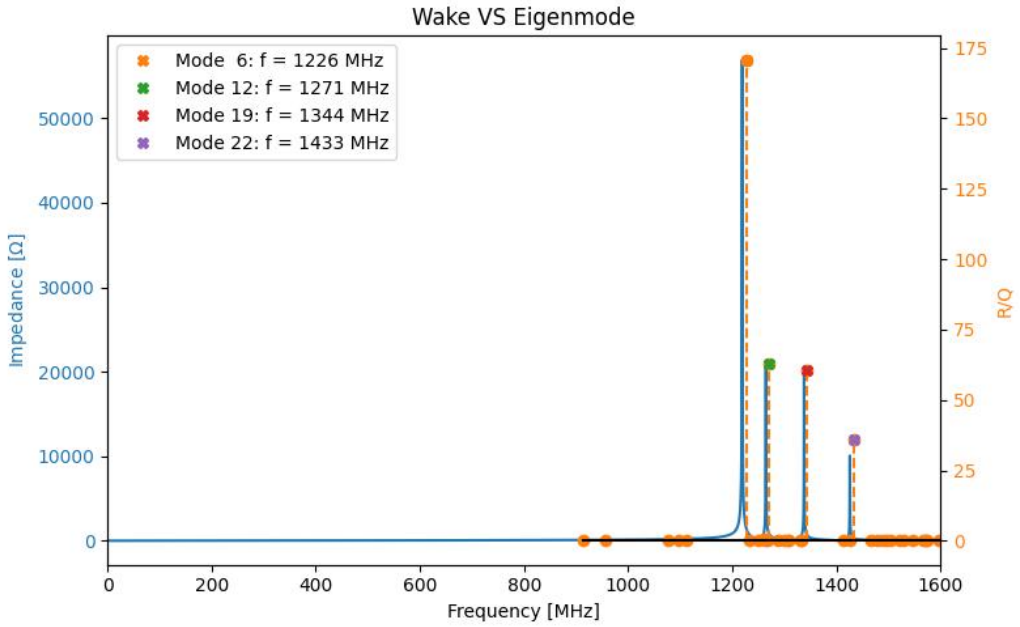

Figure 8: Empty manifold Impedance vs R/Q.

Table 1 shows the detected relevant modes and their corresponding parameters. With this information the beam dynamics team can study the impact of each mode in the performance of the accelerator and determine if corrections have to be made, i.e. if the modes have to be suppressed or attenuated.

Mode No.	Frequency [MHz]	Shunt impedance [Ω]	Quality factor	R/Q
6	1226	4017321	23524	170.8
12	1271	1662821	26492	62.8
19	1344	1745425	28837	60.5
22	1433	1115934	30954	36.0

Table 1: CST Eigen mode simulation results (manifold empty).

2.2.2 *RF Measurements*

Whenever possible, real RF measurements are carried out on the component being evaluated. For this case there was a decommissioned manifold unit that was modified to be used for laboratory measurements (the beampipe that passes inside the magnet was shortened). Figure 9 show a picture of the manifold unit used for the RF measurements.

The measurement performed is the so called probe measurement. It consists of using a two port VNA (vector network analyser) together with two RF probes that are inserted in the device under test. These probes are essentially 2 antennas (figure 11a) that allow the measurement of the electric field at different points in the device. Figure 10 shows the setup of this probe measurement for the manifold unit.

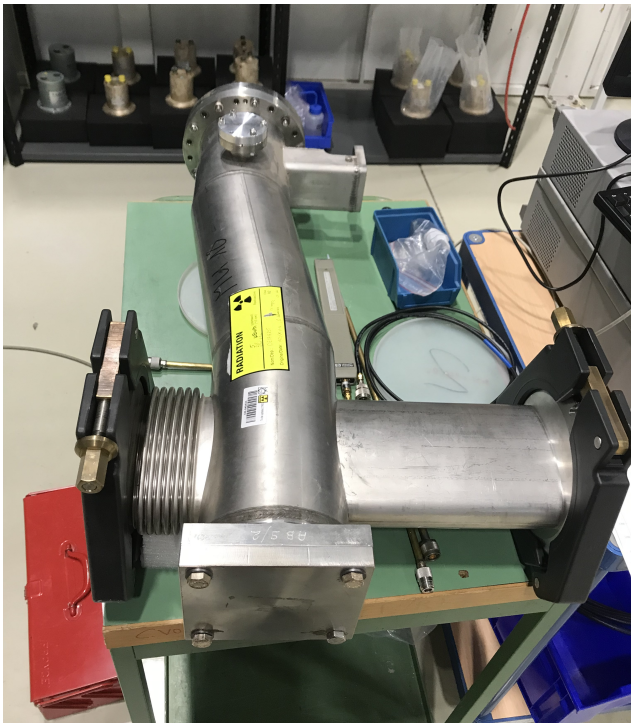

Figure 9: Decommissioned manifold used for laboratory measurements (flange covers installed).

To be able to perform the measurement, it is necessary to close all the openings of the manifold using flange covers, as can be seen in Figure 9, however, the flange covers used in the beam pipe and bellow have a hole and a probe holder to allow the RF probes to be inserted and its position secured (see figure 11b).

To start the measurement, the VNA is set to see the S-parameters in pairs in two separate windows, the top window shows reflection parameters (S_{11} and S_{22}), and the bottom window to see the transmission parameters (S_{21} and S_{12}) The start and stop frequencies are set to 1 MHz and 1600 MHz respectively. With this settings and the probes fully inserted there will be multiple resonant peaks visible on S_{21}

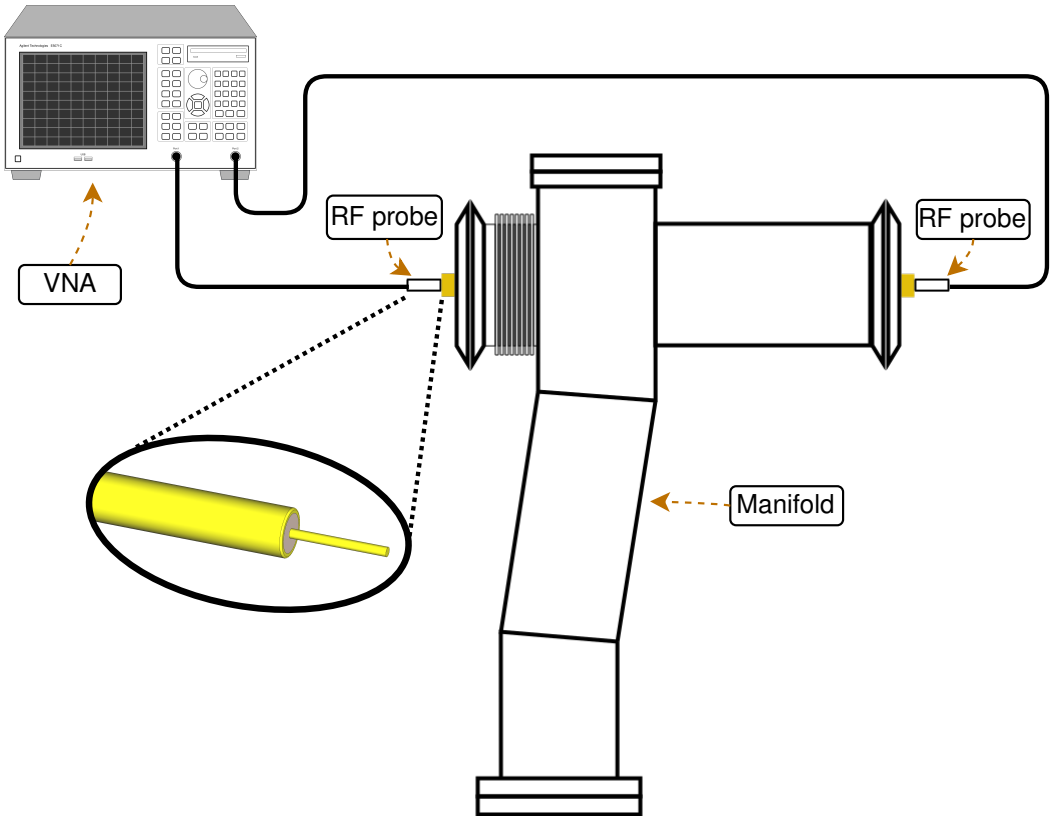

Figure 10: Probe measurement setup

and S_{12} traces, however not all resonances seen are "true" resonances coming from the device. The next step is to look at one resonance peak at a time and slowly starting to move the probes (pulling them out), if it is observed that the peak suffers a significant shift in frequency, either positive or negative, that resonant peak is considered a probe mode (not a "true" resonance). These probe modes (also called self-resonant) are excited by the coupling between the two probes and not the DUT itself and hence they are discarded.

However, if by moving the probes, the peak does not shift in frequency and only changes its amplitude, this means that the resonance is a "true" resonant mode, and the amplitude change is due to a change of the coupling to the mode. When a true resonant mode is detected, the span in the VNA is reduced to zoom in that peak and then check how strong is the probes coupling, (by looking at the amplitude of the dip in the S_{11} and S_{22}). If the amplitude of either S_{11} or S_{22} is higher than 100 mdB the corresponding probe has to be moved to keep the amplitude bellow this value. What this does is to make sure sure there is no probe mode interfering with the true resonant mode. When the coupling of both probes is bellow 100 mdB the frequency and Q value of the resonant peak (S_{21} or S_{12}) as well as all S-parameters are saved to a touchstone file.

The steps just described are repeated for every peak seen in the full span view and in the end a measurement report is written with this characterization of each

(a) RF probes

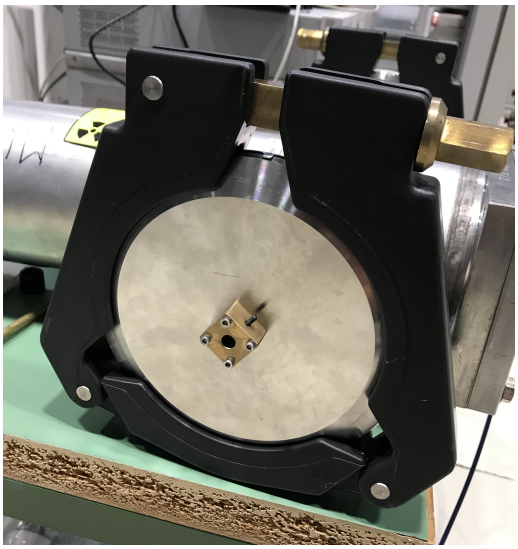

(b) Bellow flange cover with RF probe holder.

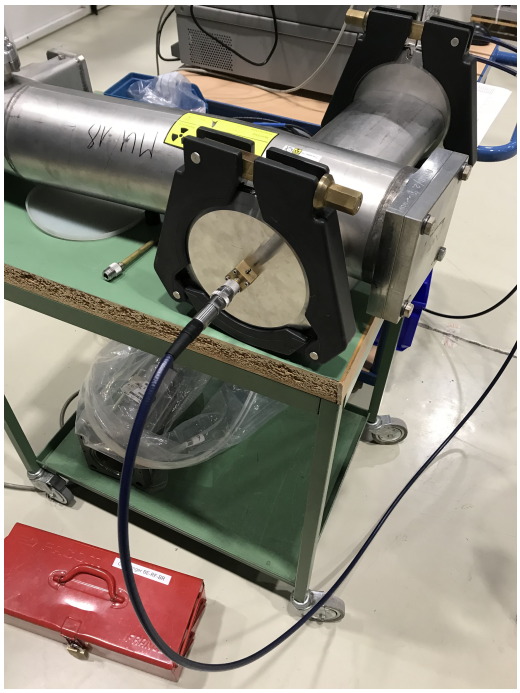

(c) RF probe inserted, bellow side.

(d) RF probe inserted, beam pipe side.

Figure 11: Laboratory RF measurement of the manifold unit.

detected peak, together with simulation data, if it exists. This report is then appreciated by the beam dynamics team at CERN to evaluate the overall impact of this resonances in the accelerator.

The Q value of a resonant peak is calculated from one of the transmission parameters, due to the fact that usually this is the trace with less noise and both S_{21} and S_{12} are equal. Plots of Figures 12,13 and 14 show some of the measured resonances (for the empty manifold) and each represent different scenarios that can happen during the measurement.

The plot of figure 12 shows a resonance at about 1118 MHz and, as can be seen, both S_{11} and S_{22} traces have a dip. However, the S_{22} trace has a weaker coupling compared to S_{11} which makes it extremely noisy, if the Q value would have been taken from this trace it would've resulted in a much more inaccurate value. Despite the fact that the S_{22} is noisy, the traces in transmission are relatively clean around the resonant peak, and the transmission trace can be used for determining the Q-value.

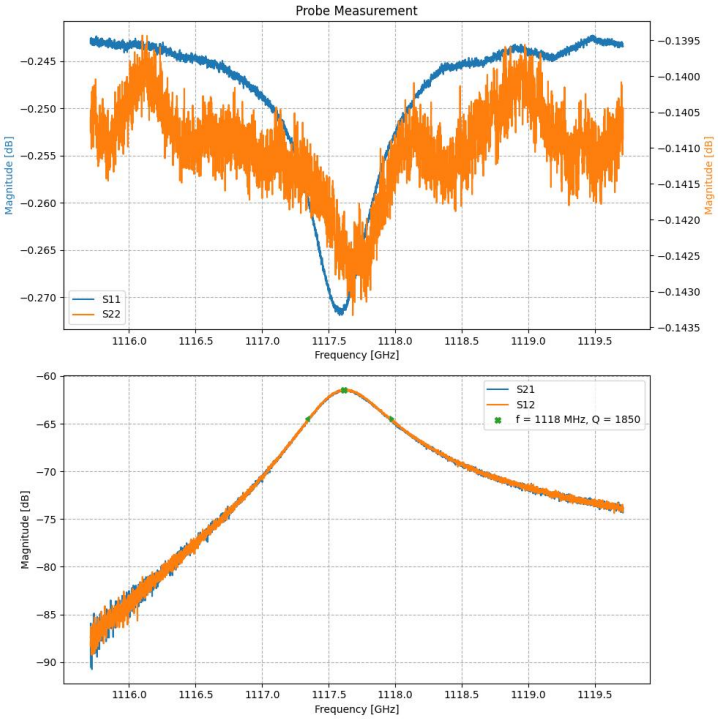

Figure 12: Probe measurement mode at 1118 MHz (manifold empty).

The plot of figure 13 shows a resonance at 1338 MHz. This measurement is an example of the best case that can happen, where both reflection parameters show a relatively low-noise dip with good coupling and exactly at same frequency.

The plot of figure 14 shows a resonance at 1437 MHz, and in this case the S_{11} trace is more noisy and the sides are sloped, and the S_{22} trace does not have a well defined dip. The S_{22} shape most likely indicates that there is a very close interfering resonance, either a true one or a probe mode. Some times it happens that the probe modes are spaced in a way that is very difficult, or even impossible, to move them away to reduce the interference. In this case, even though both reflection traces are not good, it is still possible to get the resonance frequency and Q-value from the transmission traces, as they show a well defined peak with low noise.

Figure 15 shows a plot that contains an overlay of both wakefield and eigen mode results, together with the probe measurement results. The measured modes 2, 3 and 4 are a close match (in frequency) to the three higher frequency peaks of the simulations. Small deviations in frequency are to be expected because of the

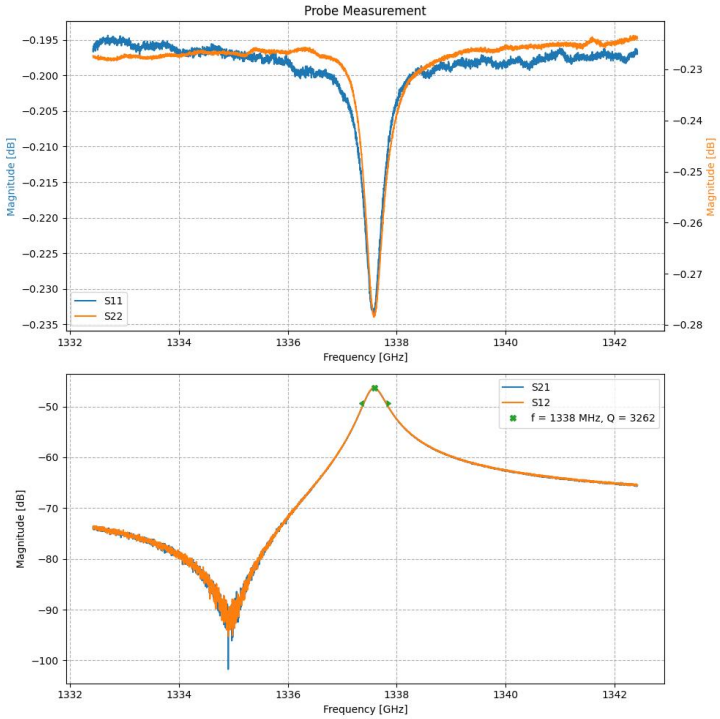

Figure 13: Probe measurement mode at 1338 MHz (manifold empty).

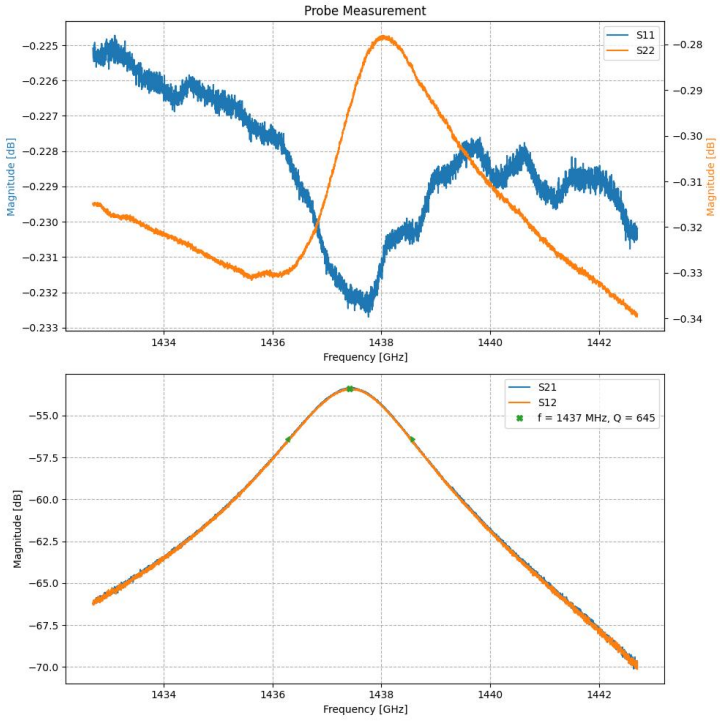

Figure 14: Probe measurement mode at 1437MHz (manifold empty).

fact that the probes are inserted in the device, and they may cause disturbances. The extent of this disturbances will depend on how the resonant mode electric field is distributed/configured inside the manifold. The measured mode 1 is not closely matched to the first mode of the simulations, this could be due to various reasons. It could in fact correspond to the first mode of the simulations, and its

field configuration is such that the insertion of the probes cause this significant shift in frequency. Another possible explanation could be that it does not correspond to the first mode, due to the probes either being completely shorting the field, or the RF probes can not reach the field of the corresponding mode . If it happens to be this last case, the measured mode 1 could be a completely different mode and the reason it does not show in wakefield simulations is because it is a mode that is not interfering by the beam.

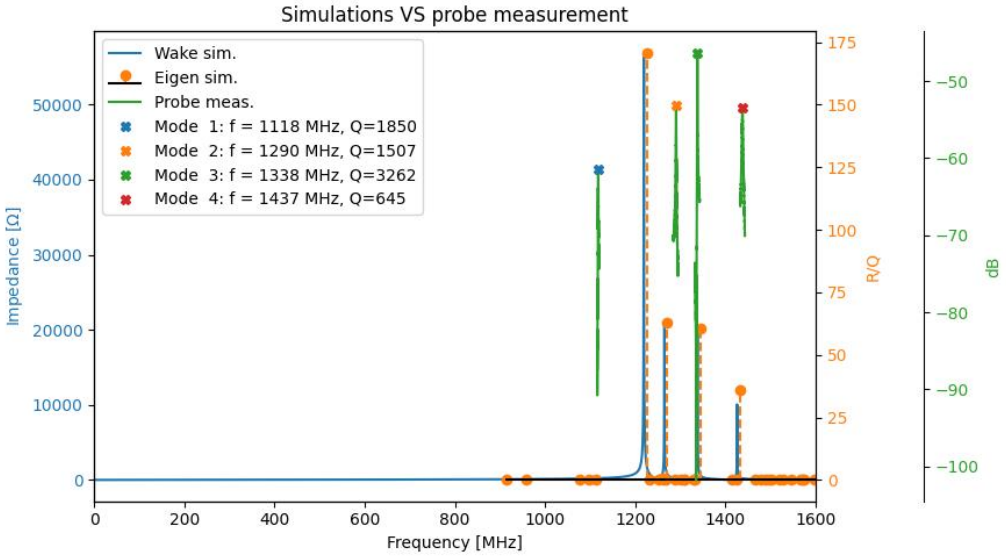

Figure 15: Probe measurement results compared to simulations (manifold empty).

2.3 MANIFOLD WITH CODD ELEMENT

As described before, the CERN PS accelerator has 55 beam instrumentation devices that are installed inside the vacuum manifolds, and they are divided as follows:

- Electrostatic pickup units:
  - Standard (x40)
  - Large (x12)
- Actuator of SEM Grid Detector (x3)

The scope of this work is focused on the pickup unit of the standard type. This electrostatic pickup unit is part of the PS Closed Orbit Digital Display (CODD) system, which is used to measure the horizontal and vertical beam position during the PS acceleration cycle. This pickup unit will be referred as CODD element, or simply CODD, in the remainder of this document.

Figure 16 shows a picture of a real CODD element inside a protective acrylic case. When assembled in the manifold the body of the CODD is electrically isolated

from the manifold structure, this is achieved because the flange of the CODD has an enamel coating and it is secured to the manifold using screws with insulating washers. Sub-figure 16b shows, with more detail, the opposite side of the CODD that has the RF contacts, also referred as RF fingers, and the ferrite blocks underneath. This ferrite material is of the 8C11 serena type, which has good RF absorption properties. The RF fingers provide contact between the ferrite blocks and the body of the manifold. Both RF fingers and ferrite blocks are attached to the CODD body using screws with insulating washers.

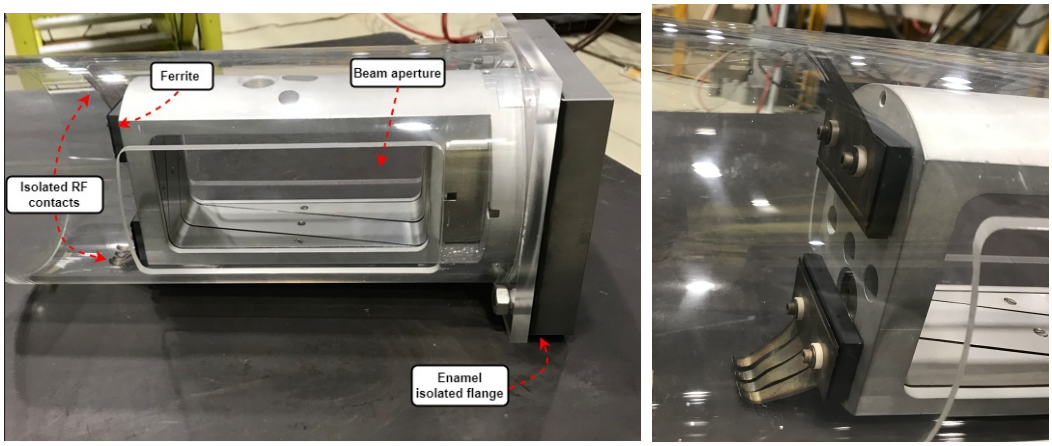

(a) (b)

Figure 16: Picture of a CODD element used for lab measurements. (a) full view; (b) Detailed view of RF contacts and ferrite blocks.

2.3.1 *CST Simulations*

Figure 17a shows the corresponding CODD CST model. In this case the 3D modeling had to be done from scratch because only 2D drawings were available. However, the modeling was done already with simplifications in mind. The material of the flange of the CODD was defined as porcelain, in reality the flange has only a thin enamel coating. The RF fingers were modeled as a single solid contact due to the fact that the gap between fingers is so narrow that it would require millions of additional mesh cells. The electrodes inside the aperture of the CODD were not modeled, again because of the narrow gap between contacts. Sub-figure 17c shows the complete CST model with the CODD element inserted in the manifold.

The wake field simulation results can be seen in figure 18, which shows a significant attenuation of the four main resonance peaks, comparing to the case of the manifold without a CODD element installed. This attenuation is more evident in the plots of figure 19 where the impedance data of the manifold empty case is overlaid with the one with the CODD installed.

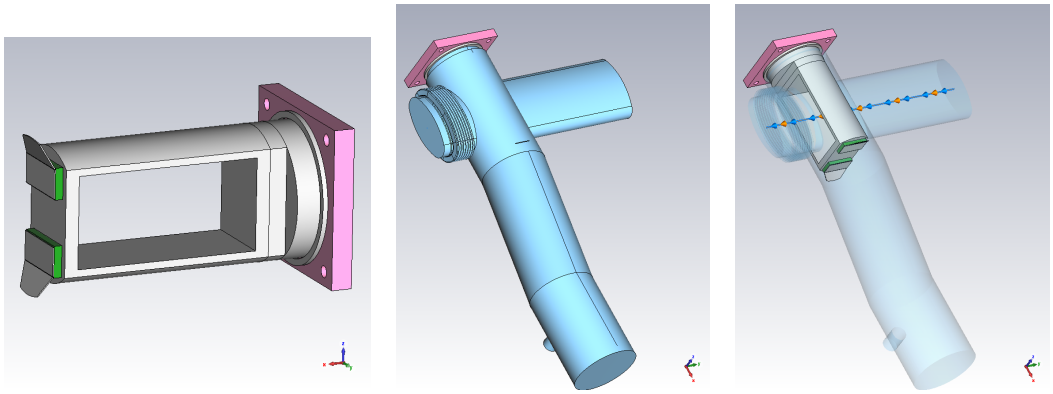

(a) CODD CST model. (b) Vacuum fill. (c) Vacuum fill.

Figure 17: CST model of vacuum manifold with CODD element.

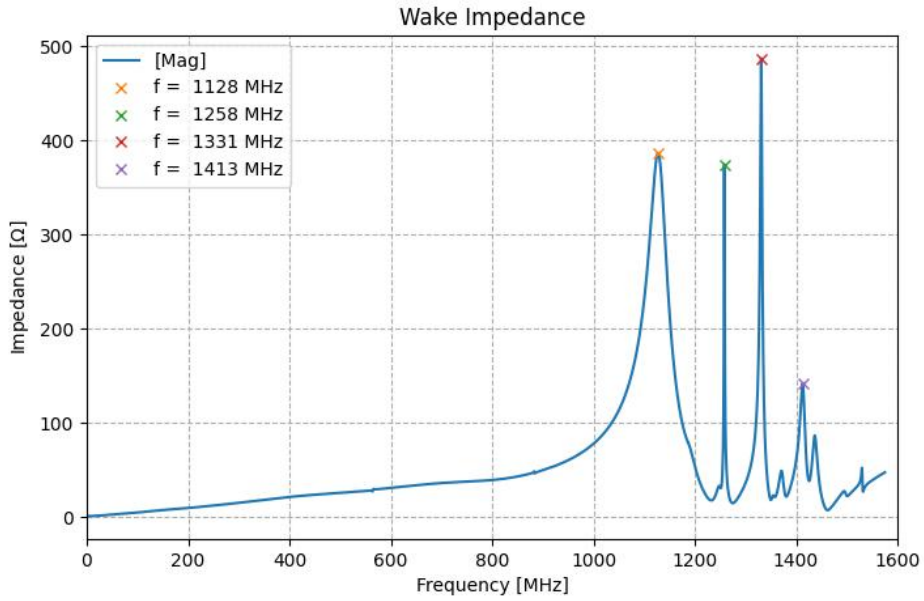

Figure 18: Impedance simulation result of manifold equipped with CODD element.

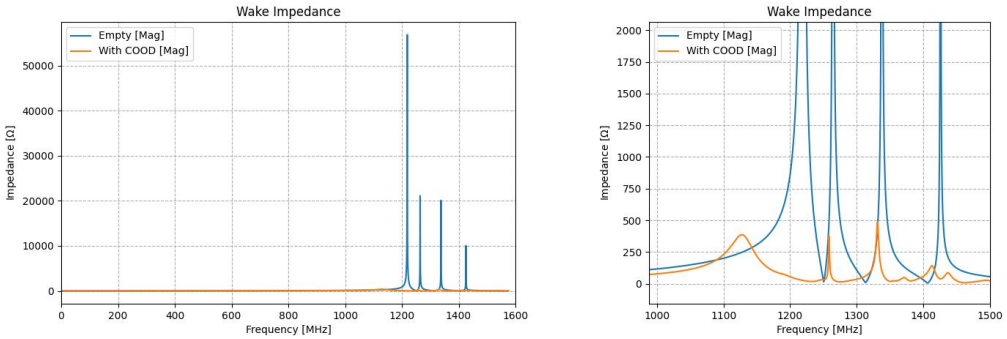

(a) (b) zoomed.

Figure 19: Impedance comparison between manifold empty and manifold with CODD element.

An eigen mode simulation was also carried out and both results, wakefield and eigen mode simulations, are compared in the plot of figure 20. Again it can seen that there is a slight shift in frequency, of a few MHz, in the detected peaks.

Table 2 shows the values of each parameter of the five relevant modes. In this simulation, an extra mode was detected at 894 MHz (mode No. 5), but given its low values of shunt impedance, quality factor and R/Q, it can be considered negligible (this is also confirmed by the fact that no impedance peak shows on the impedance trace).

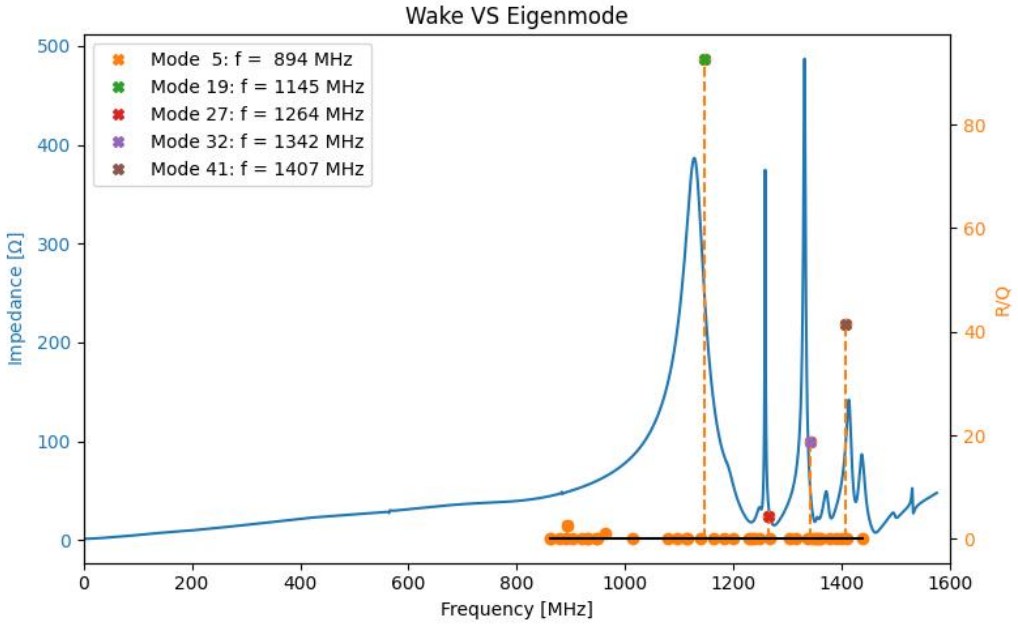

Figure 20: Impedance vs R/Q of manifold equipped with CODD element.

Mode No.	Frequency [MHz]	Shunt impedance [Ω]	Quality factor	R/Q
5	894	0.4	0.15	2.5
19	1145	204	2.2	92.7
27	1264	669	156.6	4.3
32	1342	4011	214.8	18.7
41	1407	1074	25.9	41.4

Table 2: CST Eigen mode simulation results

Despite the fact that the main goal of the CODD element is to be able to measure the position of the beam, the reality is that its presence in the manifold makes it also behave as a shield. In this case the impedance contribution of each CODD element to the overall impedance of the PS machine is unavoidable, as there is no easy or practical way to shield the resonances further without compromising the beam position measurement. As such the wake impedance of the manifold with the CODD element will serve as a baseline to benchmark subsequent shield proposals to be fitted in the manifolds that are empty.

2.3.2 *RF Measurements*

The same probe measurement setup (fig.10) was repeated, as there is a spare CODD element available for laboratory measurements. The simple square flange cover, from the measurement of the empty manifold, was removed and the CODD element was inserted and secured using four bolts with insulating washers, to keep the CODD element electrically isolated from the manifold, and thus fully replicating the configuration used in the PS machine.

The plots of figure 21 shows a measured resonance at 1442 MHz (see also Fig.22). This is an extreme non ideal case, as there is no dip in both S_{11} and S_{22} and the detected resonance peak in the S_{21} and S_{12} traces show a significant noise, that will result in a determined Q value with a larger error.

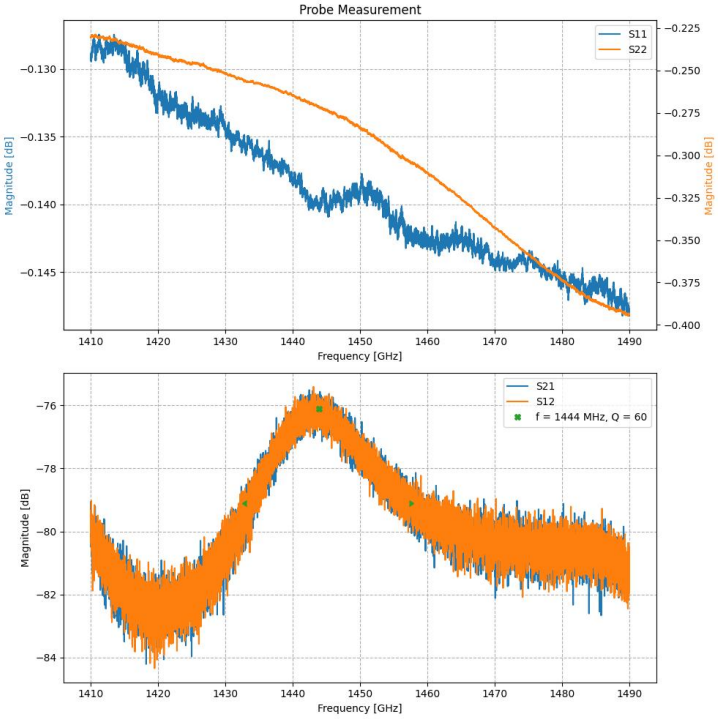

Figure 21: Probe measurement mode at 1442 MHz (manifold with CODD element).

Figure 22 shows a plot that contains an overlay of both wakefield and eigen mode results, together with the probe measurement results of the manifold with the CODD element inserted. It is possible to see that modes 2, 4, 5 and 6 are closely matched, in frequency, with the simulation results. Modes 1 and 3 have a slightly higher shift in frequency, but overall these results could be considered a good match between simulations and measurements. Also, the Q values of this measurement are much lower than the ones measured in the manifold empty case, which is to be expected due to the impedance resonant peaks being strongly attenuated in this configuration.

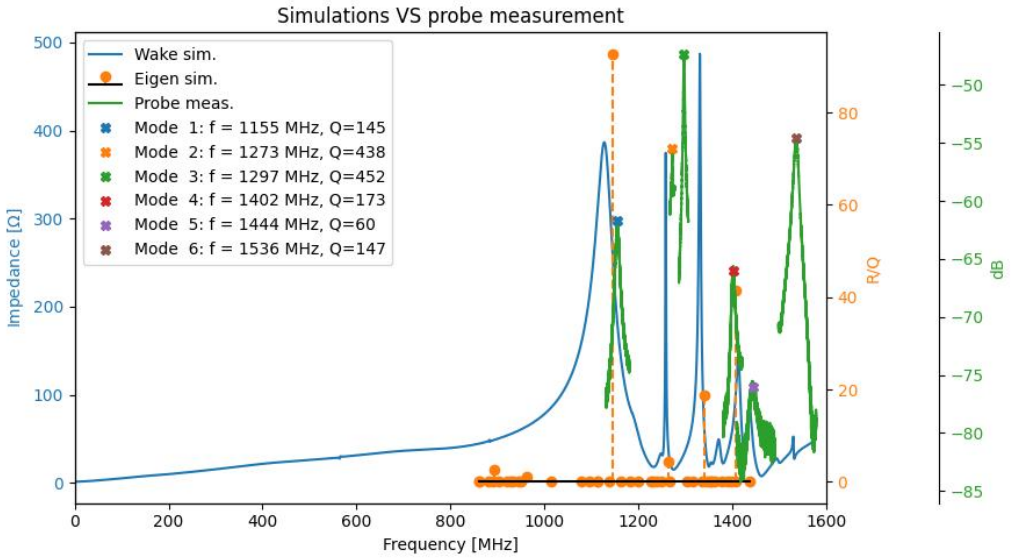

Figure 22: Probe measurement results compared to simulations (manifold with CODD element).

3

MITIGATION METHODS FOR THE PS VACUUM MANIFOLDS

The impedance contribution from the empty manifolds is quite significant, and is thought to be one contributing source to instabilities that are currently limiting the performance of the PS accelerator. There are in total 37 of this empty manifolds that could potentially be shielded and thus increasing the performance of the PS accelerator. This chapter/subchapter will be focused on the design and analysis of different shield proposals. The main principle of operation of the shields is to allow the most direct and undisturbed path possible for the beam induced image current that flows on the walls of the beam pipe, this way avoiding the excitation of wakefields.

Since the primary function of the manifold is to provide vacuum pumping access, there is a restriction for the design of the shields, that implies that they must not interfere with the pulling of vacuum. The shield performance will be compared to the impedance contribution of the CODD element that, despite not being its primary function, also provides some level of shielding.

3.1 SHIELD SOLUTION 1

The shield design proposal number 1 can be seen in figure 23. This shield is essentially a piece of perforated metal beam pipe with a width such that it makes contact with both beam pipe edges inside the manifold, this way providing a continuous structure. The body of the shield is attached through a support arm to the rectangle flange cover, which ensures that the shield stays in a defined fixed position inside the manifold. The holes in the body of the shield have a radius of 4 mm and they don't face a restriction to vacuum pumping.

Figure 24 shows with more detail how the shield is placed inside the manifold and how the contact with the beam pipe is carried out. The contact between the shield and the beam pipe is accomplished by using a cylindrical silver coated metallic spring, that was modeled as a cylinder in the required cross-sectional shape (in yellow).

With this shield installed the beam image current that is induced in the walls of the beam pipe, has an almost undisturbed path between both beam pipes inside

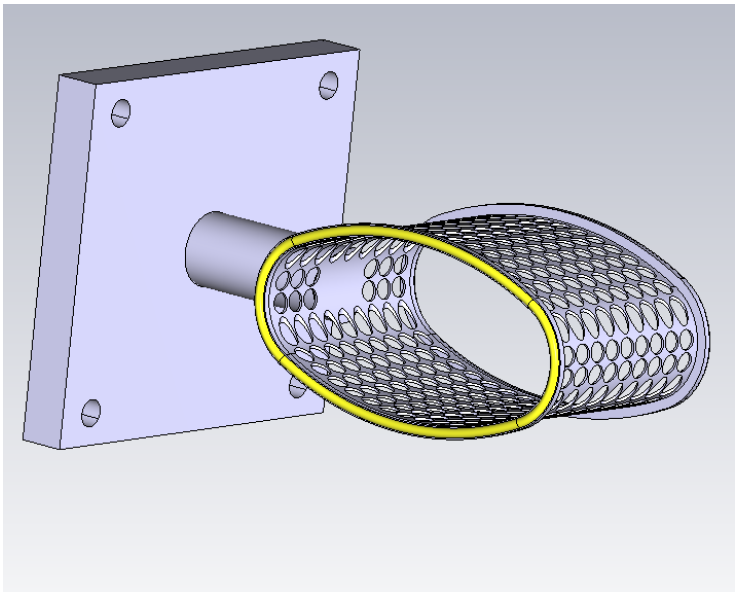

(a) Shield 1

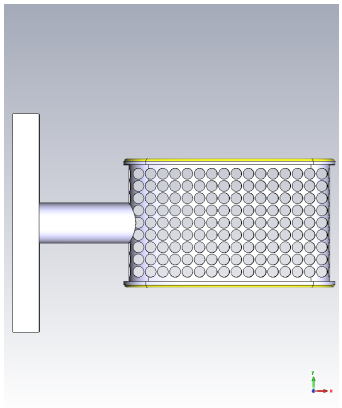

(b) top view

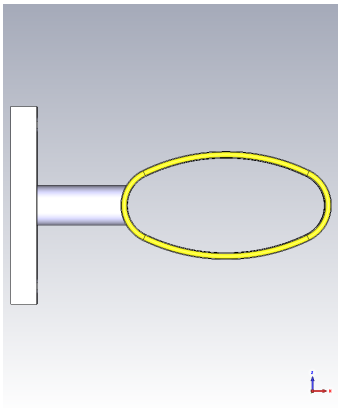

(c) Side view

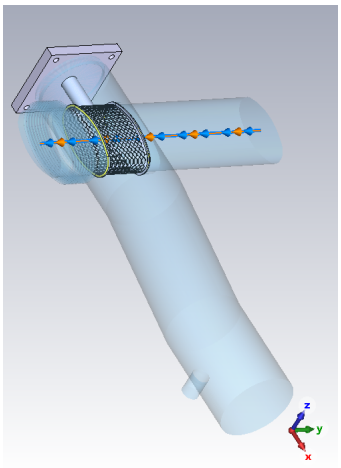

(d) CST model

Figure 23: Manifold shield proposal 1

the manifold. Being the small dip, near the RF contact spring and the weld bead of the beam pipe, the major discontinuity in this configuration, which is several orders of magnitude smaller than the discontinuity created when there is no shield.

The CST model of the manifold with shield solution 1 installed (fig. 23d) was simulated and the results of both wakefield and eigen mode simulations are shown in the plot of figure 25. As can be observed this shield is very effective at preventing the excitation of wake-fields which prevents the resonances from building up. Despite its good performance, the wakefield results still show a small resonance at 1408 MHz with an amplitude that is several orders of magnitude smaller when compared to the manifold without shield. This small resonance did not appear in the eigen mode simulation, it does not have a relevant R/Q (it will not interfere with the beam).

The plot of figure 26 shows the overlay of the impedance contribution from the manifold equipped with CODD element and the manifold equipped with shield 1.

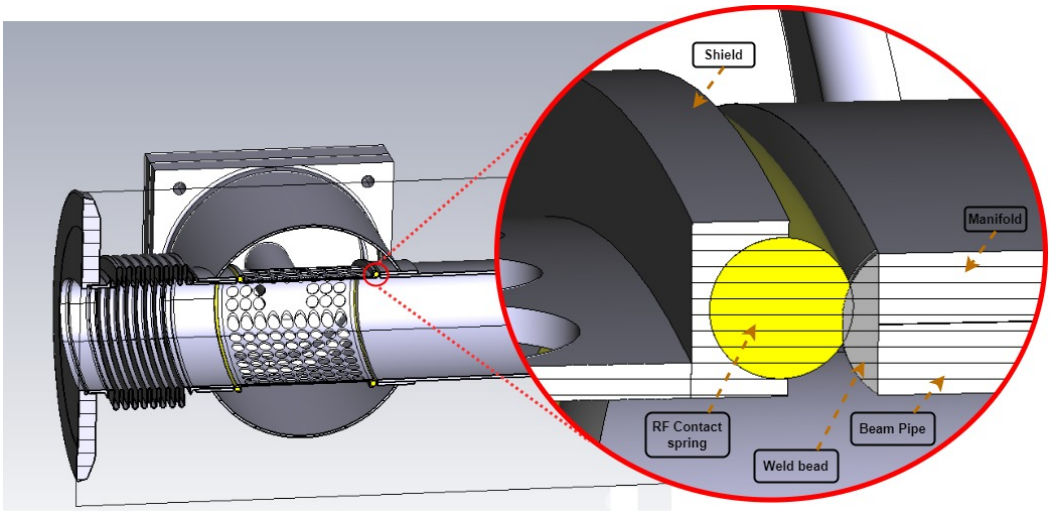

Figure 24: Shield 1 installed in the manifold

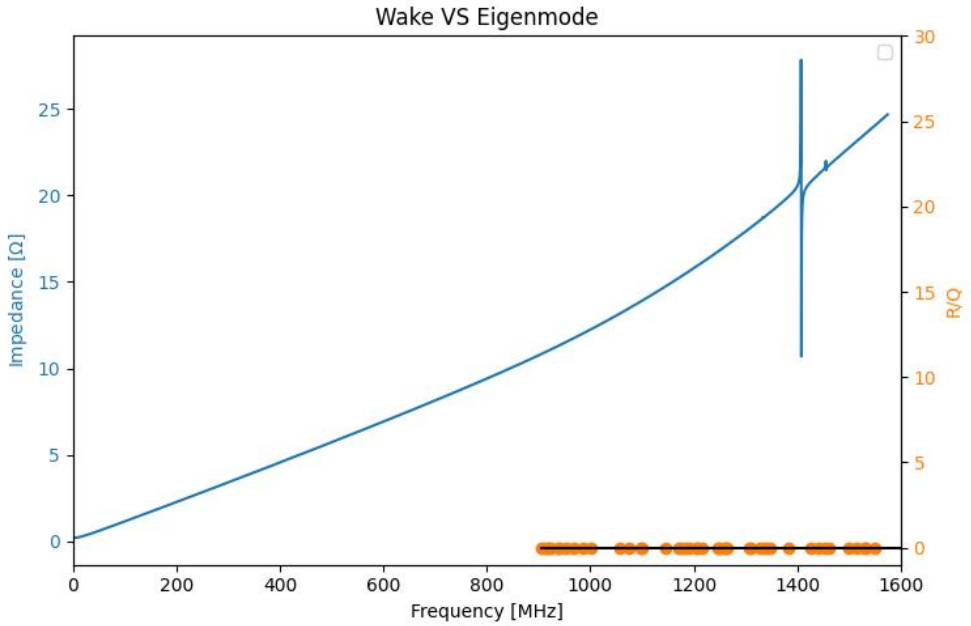

Figure 25: Wakefield and Eigen mode simulation results for manifold equipped with shield solution 1.

This shield design proposal was discussed with the CERN's vacuum team, which is the team responsible for these manifolds, and they informed us that even though the performance of the shield is excellent, they would prefer a simpler solution to be installed for practical reasons. This is motivated by the fact that the shield has a fixed width, and the distance between the beam pipe openings inside of the manifold is varying from manifold to manifold. There are situations where it is necessary to remove and separate the manifold chamber from the beam pipe that sits inside the bending magnet, and this is achieved by cutting the weld bead shown in figure 24. When re-assembling is done a new weld is made, which subsequently would require a shield with an increased width to cover the increased distance. This is of course

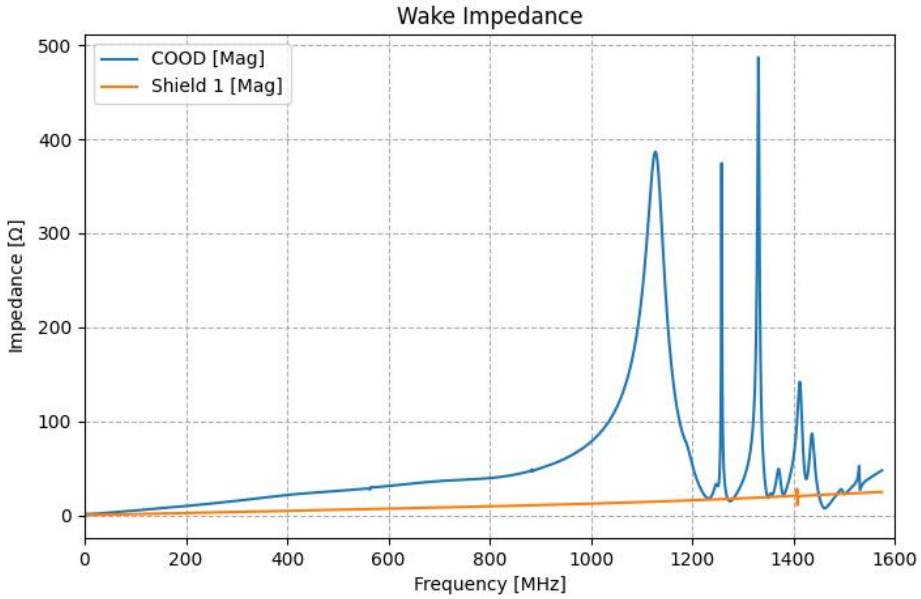

Figure 26: Comparison of simulation results between manifold with CODD element and manifold equipped with shield 1.

impractical as in the worst case scenario every manifold may require a custom made shield.

3.2 SHIELD SOLUTION 2

Figure 27 shows the shield design proposal number 2. In this version the shield solution does not require a support arm to be attached to the flange cover, as the contact is made on the outside and all around of the beam pipe openings, contrary to shield solution 1 where the contact was made directly on the edge. Essentially, a small length of the beam pipe openings sits inside of the shield.

The main body of this version of the shield is modeled as if it was a perforated piece of beam pipe, just like in shield 1, for simulation efficiency reasons. However, if this was to be fabricated, the main body of the shield had to be made of some kind of metallic braided/mesh material to allow it to have some degree of flexibility in the longitudinal direction. This flexibility is needed as the shield has to be compressed to install it into the manifold, and when close to its final position it is released and extended to fit all around the beam pipe openings.

Figure 28 shows, with more detail, how the shield sits when correctly installed in the manifold. The contact is made with the same type of RF contact spring as in shield solution 1. As the contact is made all around the outside part of the beam pipe, this shield has the advantage that it supports itself and is immune to the beam pipe length variations explained before.

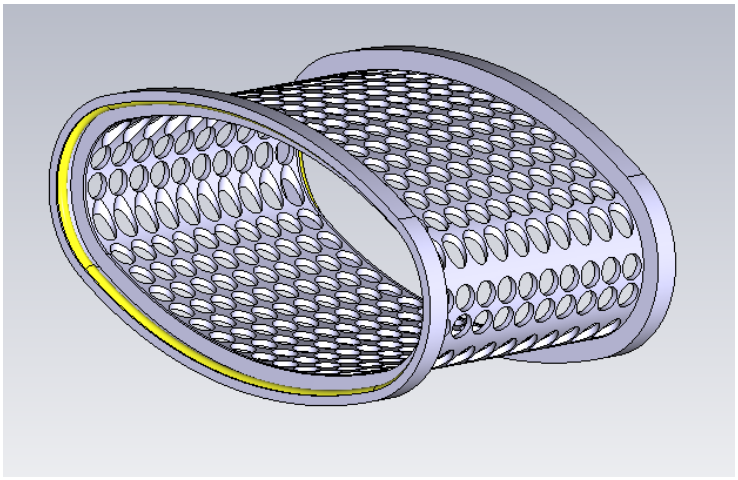

(a) Shield 2

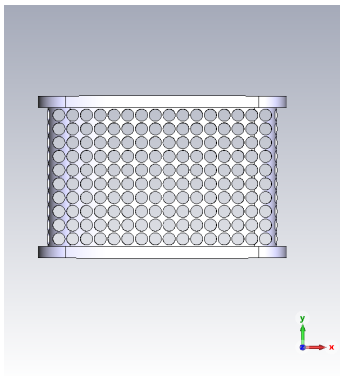

(b) top view

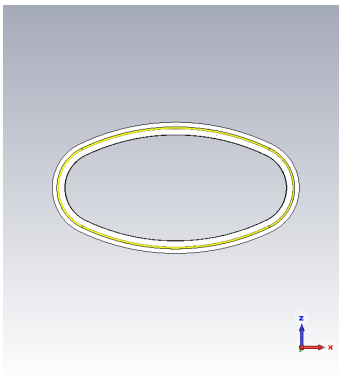

(c) Side view

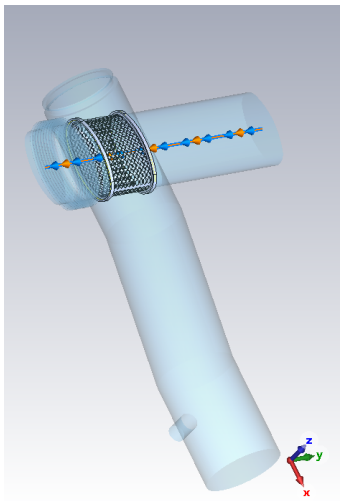

(d) CST model

Figure 27: Manifold shield proposal 2

If the weld bead inside the manifold was never cut, it is possible that the body of the shield touches the weld bead, making an additional contact point besides the RF contact spring, which is the main contact. For the simulation it was decided to leave a small gap (1mm), and this would represent the case where the manifold was already removed from the pipe and reinstalled.

The CST model of the manifold with shield solution 2 installed (fig. 27d) was simulated and the results of both wakefield and eigen mode simulations are shown in figure 29. This shield also has an excellent performance, very similar to the one of shield 1, as it was to be expected as the working principle of both are very similar. The detected peak was slightly shifted to a lower frequency of 1380 MHz.

The plot of figure 30 shows the overlay of the impedance contribution from the manifold equipped with CODD element and the manifold equipped with shield 2.

After a discussion with the CERN's vacuum team about this shield design, the feedback obtained was that this design is possible to be implemented in practice

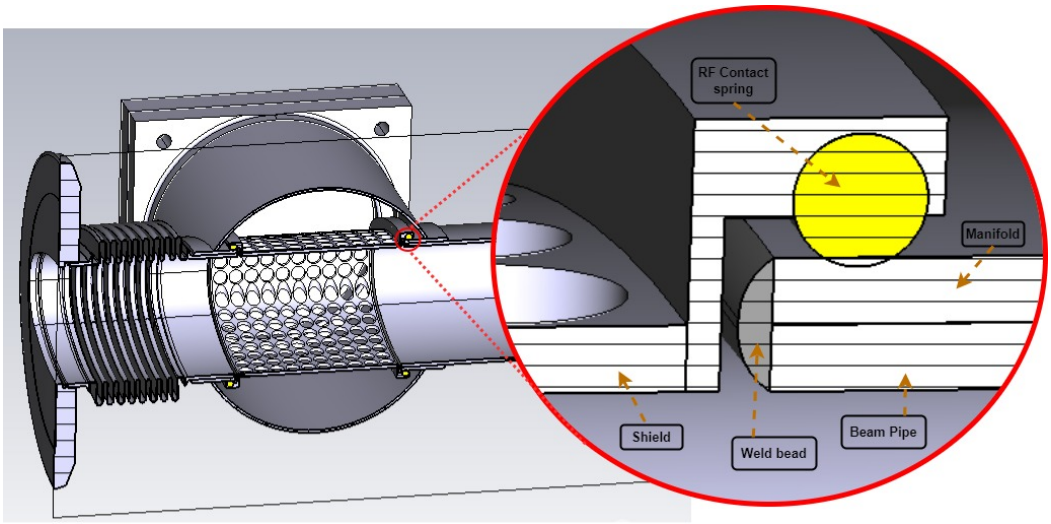

Figure 28: Shield 2 installed in the manifold

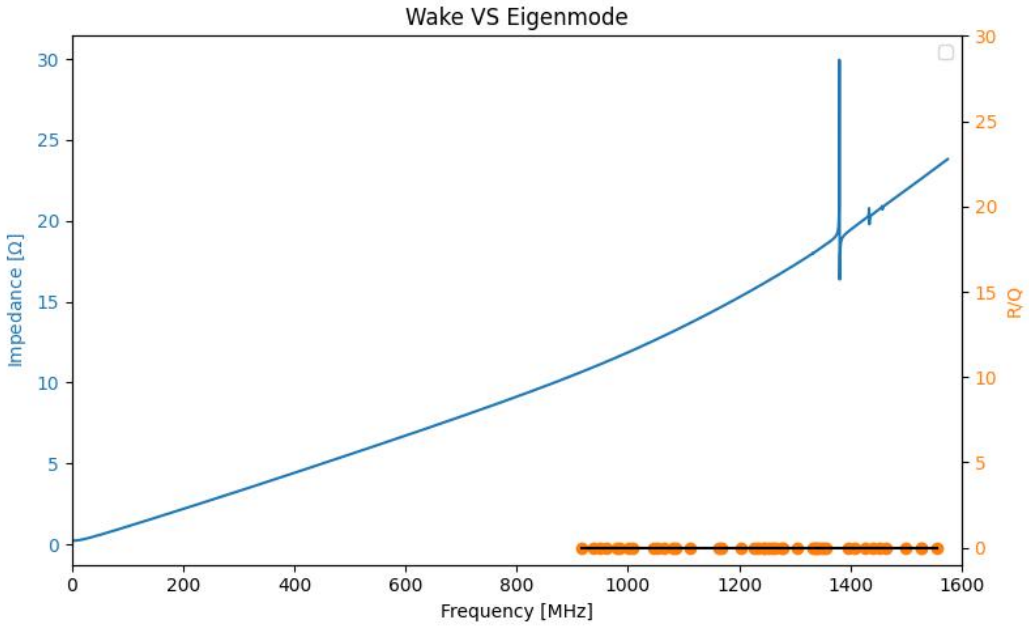

Figure 29: Wakefield and Eigen mode simulation results for manifold equipped with shield solution 2.

and does not pose a vacuum restriction. It would therefore be the preferred solution. In case that a less rigid material is selected for the body of the shield, it may be necessary to use an additional clamp on the outside of the shield. This clamp would prevent the shield from accidentally contracting or sag and potentially be hit by the beam. The clamp being on the outside of the shield would not have an influence on its performance.

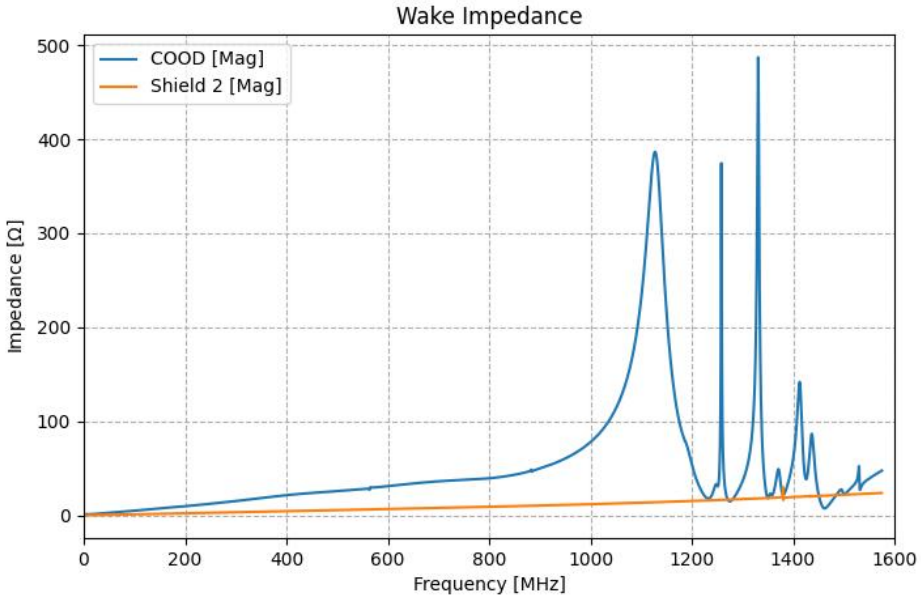

Figure 30: Comparison of simulation results between manifold with CODD element and manifold equipped with shield 2.

3.3 SHIELD SOLUTION 3

Figure 31 shows the shield design proposal number 3. The body of this shield is very similar to first design proposal and is meant to be of a fixed width, being the only difference the RF contacts. In this version the contact between shield and manifold is made with RF fingers on the outside part. The RF fingers do not cover the entire perimeter of the shield, as seen in orange in Fig.31b, because it would not be possible to insert the shield in the manifold if they were any longer, due to the fact that this shield cannot be compressed.

Figure 32 shows with greater detail how the shield sits inside the manifold. In this design there is a gap of 1 mm between the shield and the manifold, and as the RF fingers are making the contact on the outside part makes it possible to have some gap width variation without compromising the contact.

Figure 33 shows the plot with results from the wakefield simulation. As seen this shield has an inferior performance as there are four resonances at 637 MHz, 781 MHz, 1530 MHz and 1569 MHz with a significant amplitude, close to the order of magnitude of the empty manifold. The reason for this poor performance could be attributed to the fact that there remains a gap between the shield and the manifold, and the lack of RF fingers in more than 50 % of the shield contour.

An eigen mode simulation was also carried out and the results are shown in the plot of figure 34. Only one mode with a significant R/Q was detected at 791 MHz, it

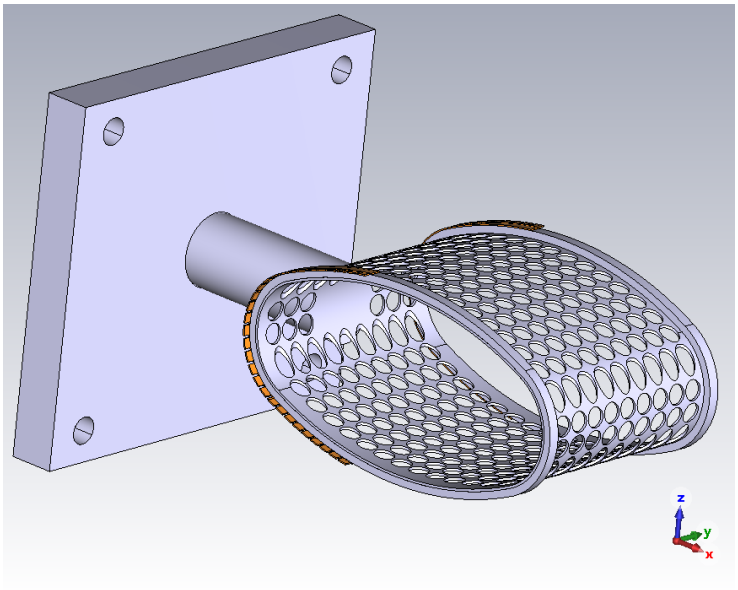

(a) Shield 3

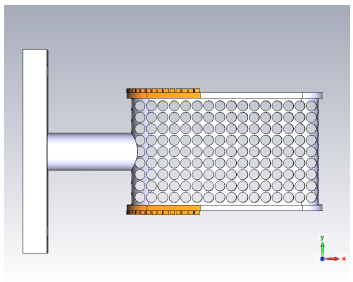

(b) top view

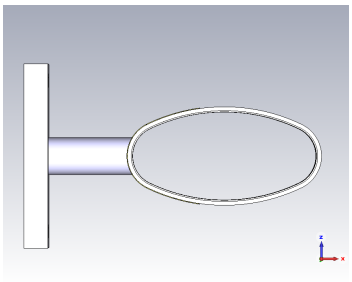

(c) Side view

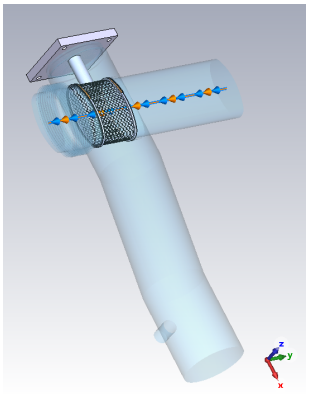

(d) CST model

Figure 31: Manifold shield proposal 3

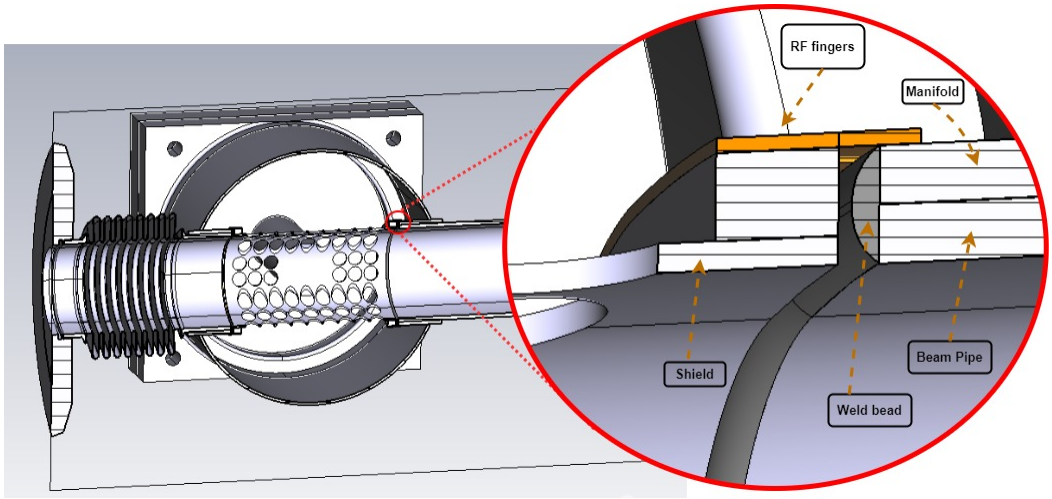

Figure 32: Shield 3 installed in the manifold

matches with the mode at 781 MHz from the wake simulation, and all its parameters are shown in table 3.

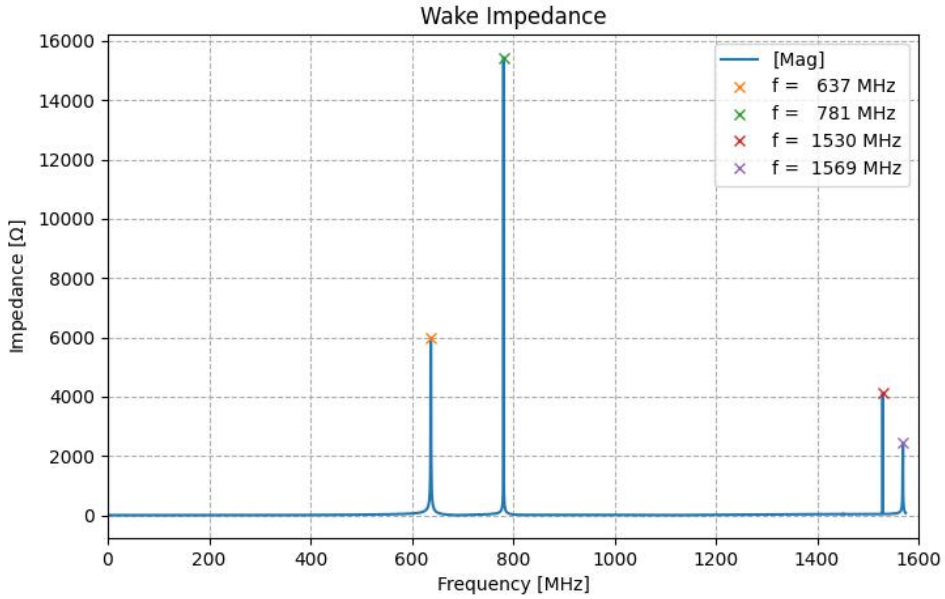

Figure 33: Wakefield and Eigen mode simulation results for manifold equipped with shield 3.

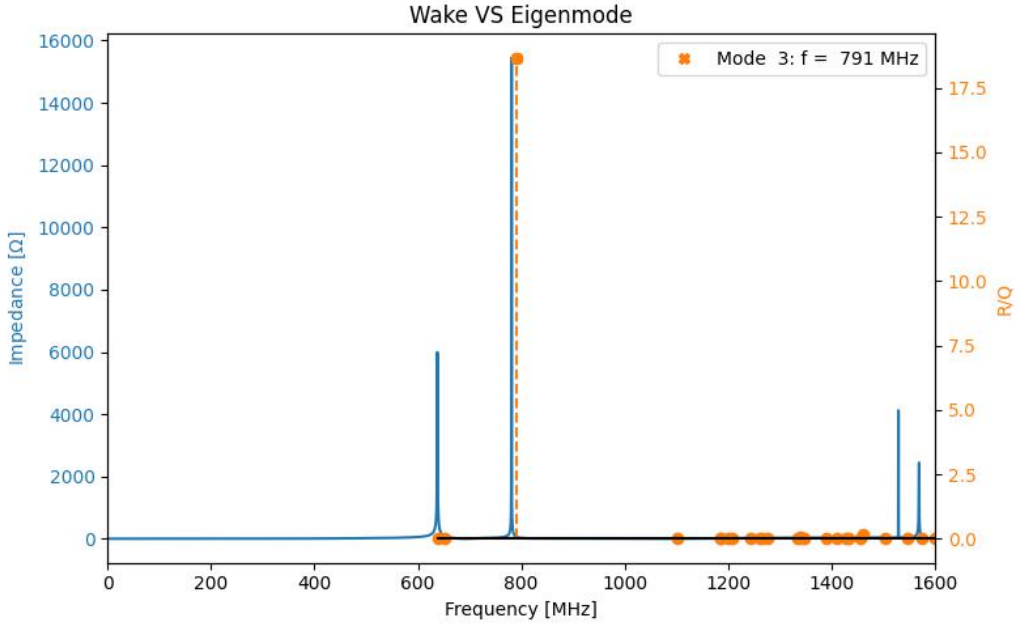

Figure 34: Wakefield and Eigen mode simulation results for manifold equipped with shield 3.

Mode No.	Frequency [MHz]	Shunt impedance [Ω]	Quality factor	R/Q
3	791	18729	1004	18.66

Table 3: CST Eigen mode simulation results for manifold equipped with shield solution 3.

The plot of figure 35 shows the overlay of the impedance contribution from the manifold equipped with CODD element and the manifold equipped with shield solution 3. As expected this shield is less performant, its shielding efect is much

worse than the CODD element. This shield is shifting two of the resonances towards much lower frequencies which may be more critical. As such this design wont be considered as a solution for the impedance mitigation in the manifolds.

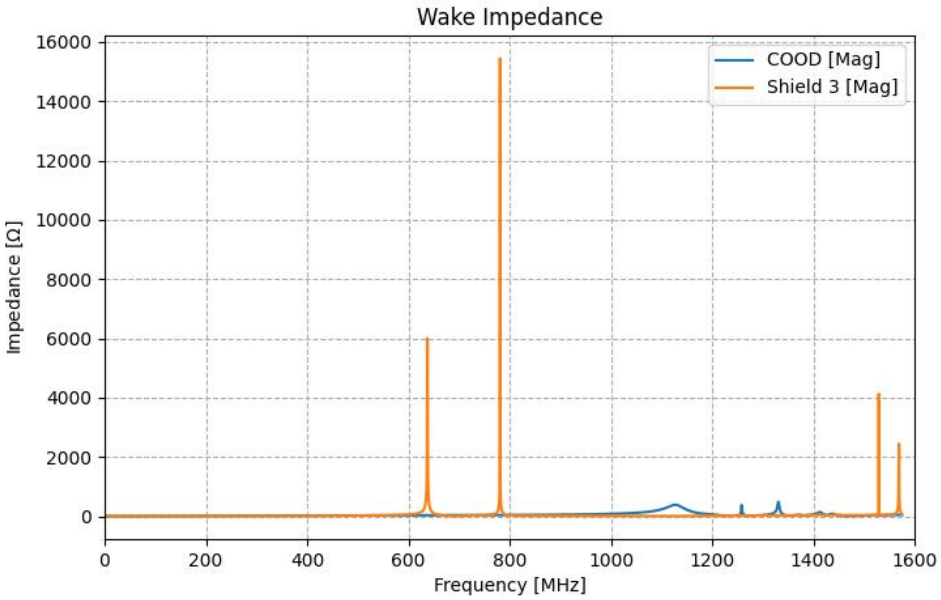

Figure 35: Comparison of simulation results between manifold with CODD element and manifold equipped with shield solution 3.

3.4 SHIELD SOLUTION 4

The shield design proposal number 4 can be seen in figure 36. Such design is essentially an iteration over shield number 3. This version of the shield consists in adding a block of 8C11Serena ferrite material together with RF fingers, on the side of the shield where the gap is opened (without RF fingers). This concept was inspired in the CODD element, however, in this shield there is no electric insulation in the flange cover.

Figure 37 shows with greater detail the shield installed into the manifold. The RF fingers attached to the ferrite block will make contact with the top and bottom of the manifold chamber.

In order to study the impact of the gap in the beam impedance, it was decided to to perform three simulations varying the gap width. The first simulation has a gap of 1 mm, the second a gap of 2 mm and the third has a gap of 11 mm (the same as the CODD element).

The plot of figure 38 shows the wakefield and eigen mode simulation results for the shield with the gap of 1 mm. A wake impedance peak is detected at 784 MHz and 1562 MHz, which matches to the ones of shield 3, however this ones have a

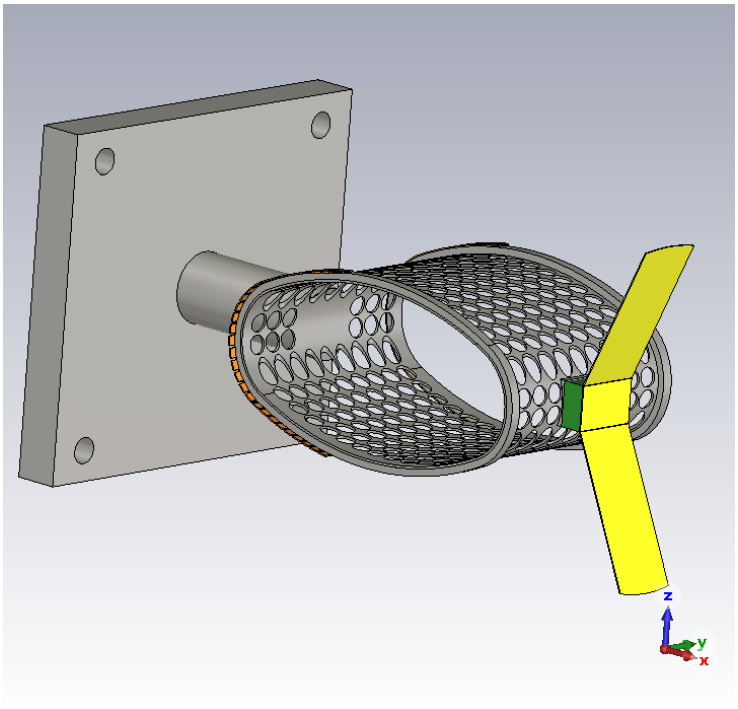

(a) Shield 4

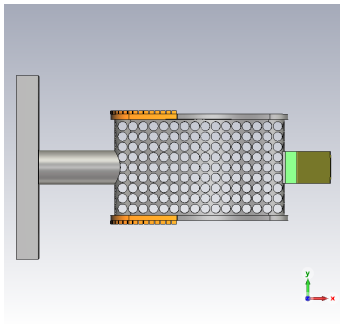

(b) top view

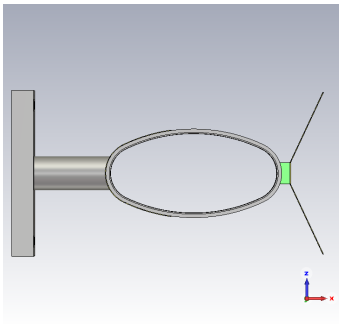

(c) Side view

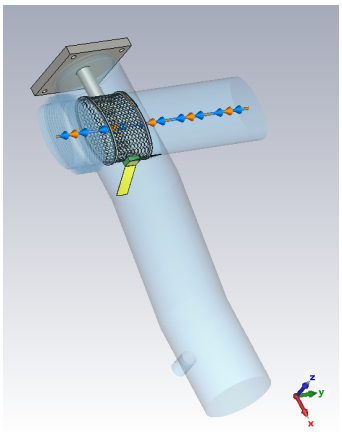

(d) CST model

Figure 36: Manifold shield proposal 4

much lower amplitude. All the parameters of the single R/Q eigen mode detected can be seen in table 4.

Mode No.	Frequency [MHz]	Shunt impedance [Ω]	Quality factor	R/Q
14	794	255	13.68	18.63

Table 4: CST Eigen mode simulation results for manifold equipped with shield 4 and a gap of 1 mm.

The plot of figure 39 shows the simulation results for the shield with the gap of 2 mm. The detected peaks have a resonance frequency of 827 MHz and 1546 MHz. With an increase of 1 mm in the gap we can see a small positive shift in the resonance frequency of the main peak and a decrease in amplitude, as well as a negative shift

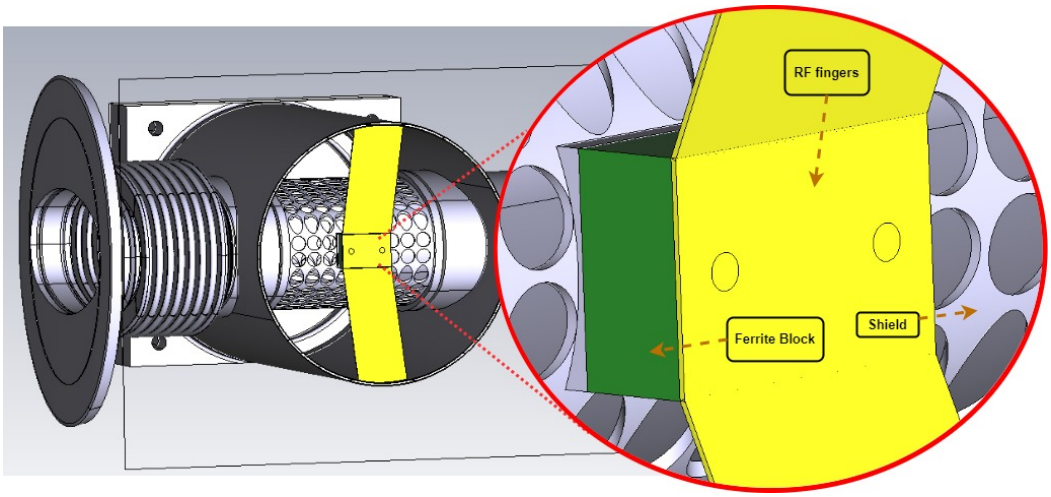

Figure 37: Shield solution 4 installed in the manifold.

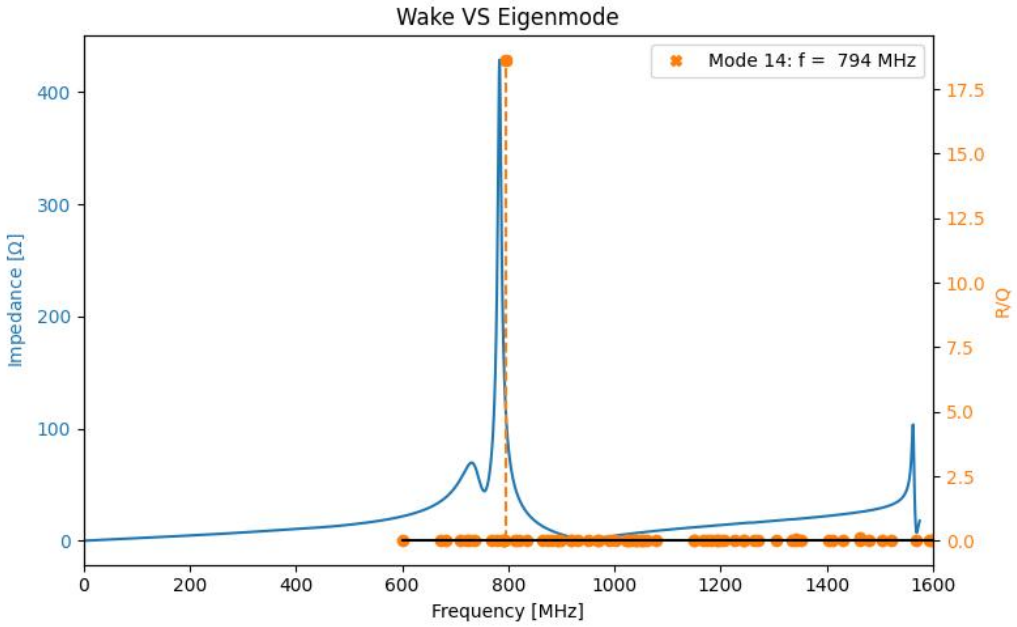

Figure 38: Wakefield and Eigen mode simulation results for manifold equipped with shield 4 and a gap of 1 mm.

and increase of amplitude for the second peak. The parameters of the matching R/Q eigen mode can be seen in table 5.

Mode No.	Frequency [MHz]	Shunt impedance [Ω]	Quality factor	R/Q
16	844	276	10.5	26.19

Table 5: CST Eigen mode simulation results for manifold equipped with shield 4 and a gap of 2 mm.

The plot of figure 40 shows the simulation results of shield 4 with a gap of 11 mm, which is similar to the CODD configuration. In the wakefiled simulation three main resonances were found at 891 MHz, 1020 MHz and 1518 MHz. Again with the further increase in the gap width, we can observe the positive frequency shift and

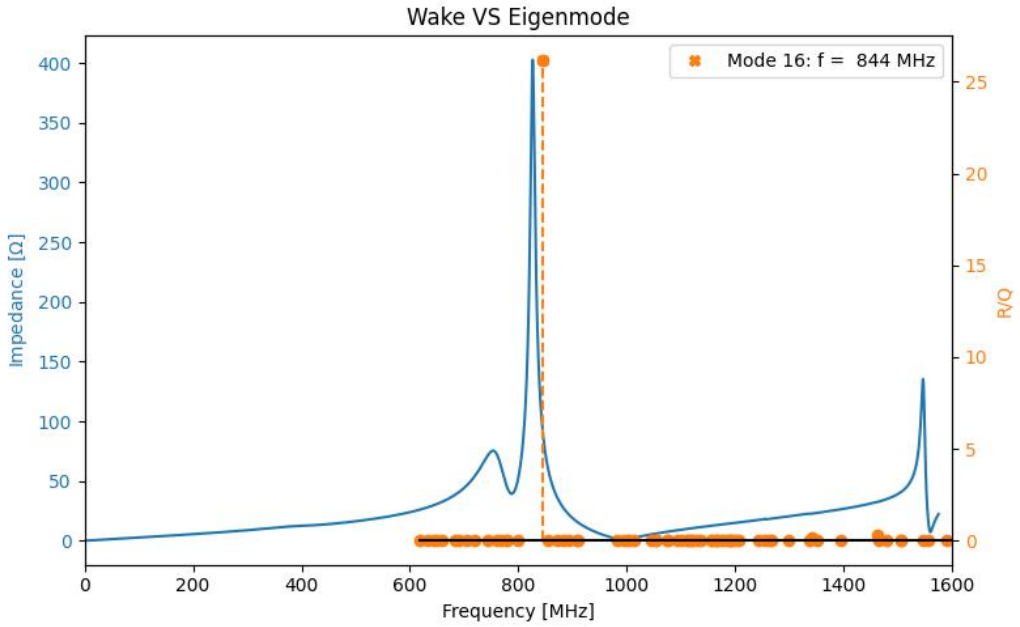

Figure 39: Wakefield and Eigen mode simulation results for manifold equipped with shield 4 and a gap of 2 mm.

decrease of amplitude of the second resonance. The parameters of the two detected R/Q modes can be seen in table 6.

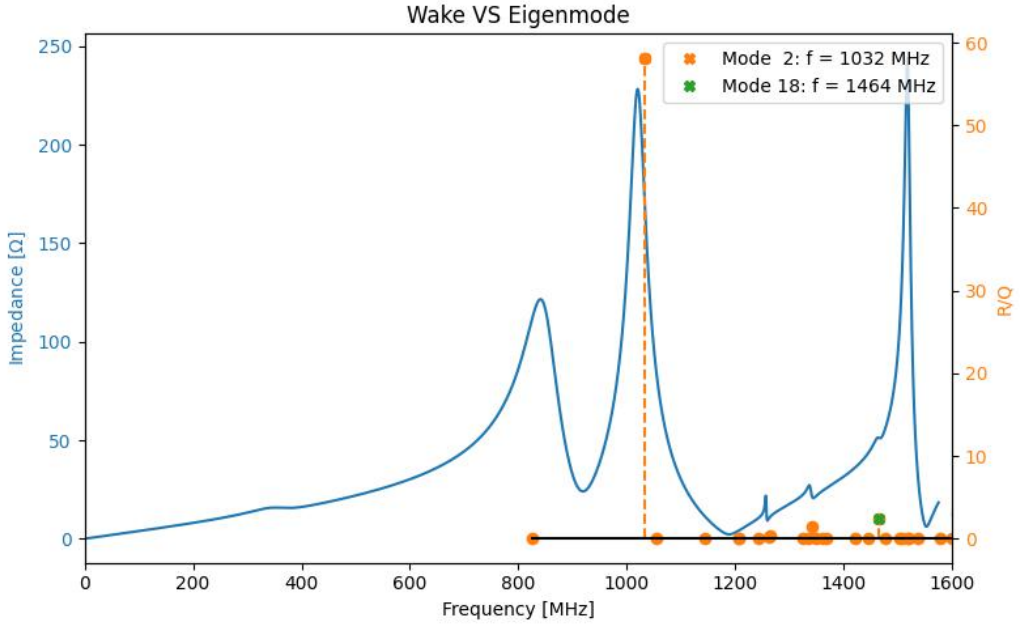

Figure 40: Comparison of Wakefield and Eigen mode simulation results for manifold equipped with shield 4 and a gap of 11 mm.

A comparison is made between the impedance contribution of shield proposal 4, with all its gap width variations, and the one from the CODD element in the plot of figure 41.

Mode No.	Frequency [MHz]	Shunt impedance [Ω]	Quality factor	R/Q
2	1032	396.4	6.82	58.16
18	1464	15.8	6.39	2.48

Table 6: CST Eigen mode simulation results for manifold equipped with shield 4 and a gap of 11 mm.

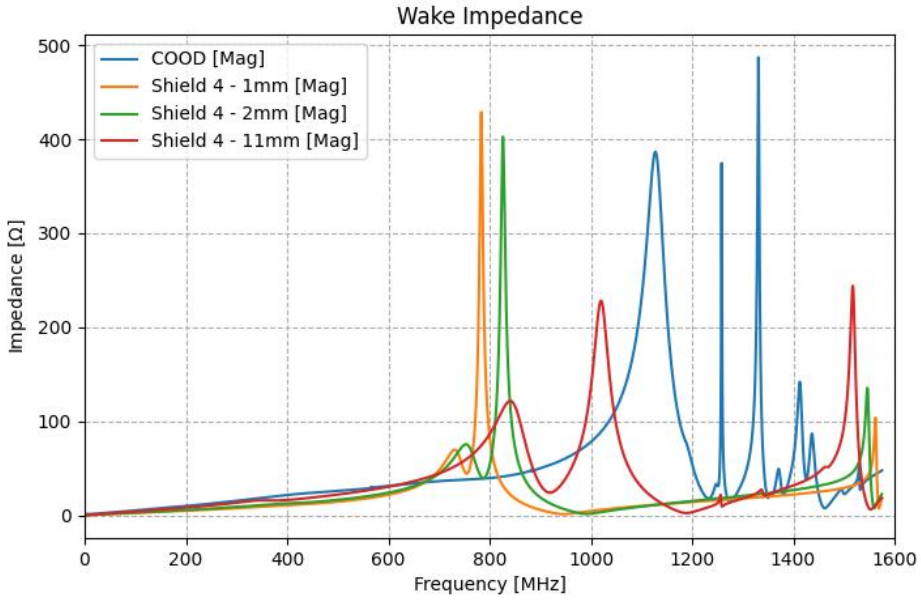

Figure 41: Comparison of simulation results between manifold with CODD element and manifold equipped with shield 4 with different gaps.

At first glance, from the three gap configurations, the shield design with a gap of 11 mm seems to be the one with the best performance. From the side of the vacuum team, this design can also be accepted for installation as it does not pose any restrictions with respect to vacuum pumping. The only potential problem could have been the ferrite material as it could cause outgassing, but this is not the case because the type of ferrite material proposed is already accepted for vacuum use (as it is the same as the one which is already used in the CODD element).

However, as this shield does not completely attenuate the resonances, and some of the remaining resonances are shifted to lower frequencies, an analysis of the results by the beam dynamics team is necessary. The reason is that the impedance budget for the PS accelerator is not constant in its entire frequency band. A resonance might be a problem at one specific frequency but if it shifts to another frequency region, it might then move into an accepteable range. Also, each of the resonance parameters like impedance, quality factor, shunt impedance and R/Q can cause different types of beam instabilities.

It was only possible to consider this shield also as a solution for the manifold resonances, without consulting the beam dymanics experts, if the calculated impedance

trace would have fallen below the impedance trace of the manifold with the CODD element. As this is not the case, a decision can only be taken after further analysis from the beam dynamics team.

3.5 EVALUATION OF SHIELD PERFORMANCE VIA ELECTRIC FIELD COMPARISON

After performing a wakefield simulation in CST, it is possible to define an electric field time monitor to get a 3D visual representation of the electric field as the bunch of charged particles traverses the manifold. As such, an electric field monitor was defined to get the field pattern from 0 ns up to 10 ns with intervals of 0.05 ns to allow a comparison of the resonant field build-up as this allows an intuitive approach to judging a shielding effect.

Figure 42 shows the electric field configuration, at 2.5 ns, 3.8 ns, 5.1 ns, and 9.95 ns from left to right respectively, for all the relevant manifold setups. Shield 1, Shield 3 and Shield 4 with a gap of 2 mm were purposely not shown, due to the fact that Shield 1 and Shield 3 wont be implemented, and shield 4 with a gap of 2 mm is very similar to the one with the gap of 1 mm. The bunch of charged particles travels through the structure of the manifold from the right side to the left.

This 3D representation of the electric field in function of time, is another way of intuitively compare and evaluate the effectiveness of the different shields. Comparing the extreme cases, the manifold empty (42a) and the manifold with shield 2 (42e), we can easily see that no resonance builds up in the chamber of the manifold equipped with shield 2, but at 9.25 ns the manifold that is empty is still showing strong resonances.

For this particular case it was easy to predict that the manifold chamber is where the resonances would build up, but this is not so straight forward for other types of equipment with much more complex geometries. For those complex cases this type of electric field calculation is useful to be able to pinpoint where exactly a potential resonance is building up.

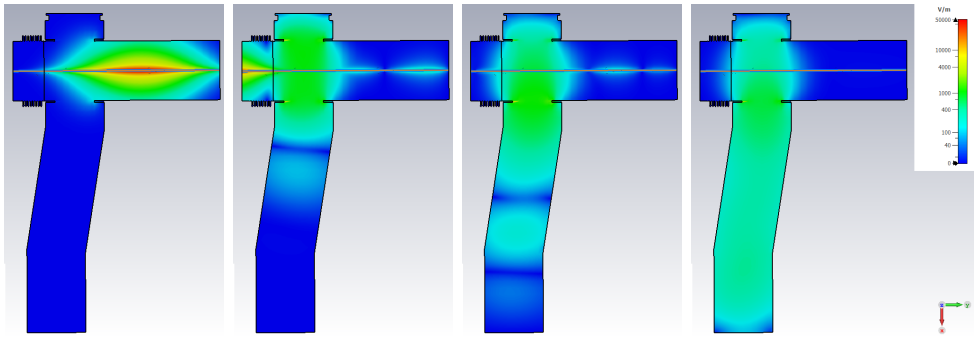

(a) Manifold empty

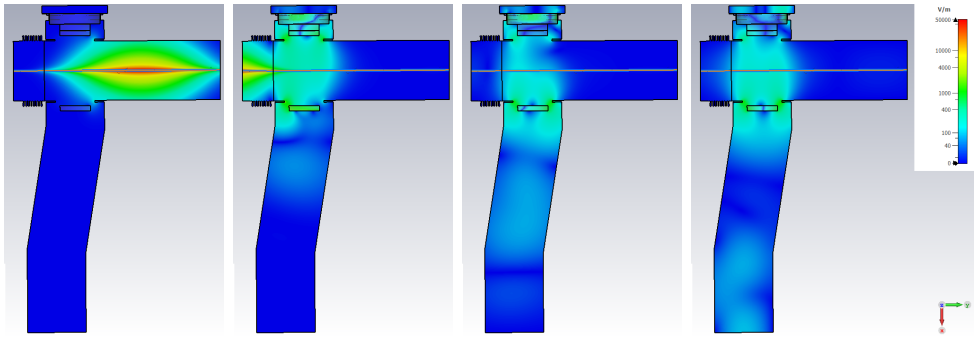

(b) Manifold with CODD

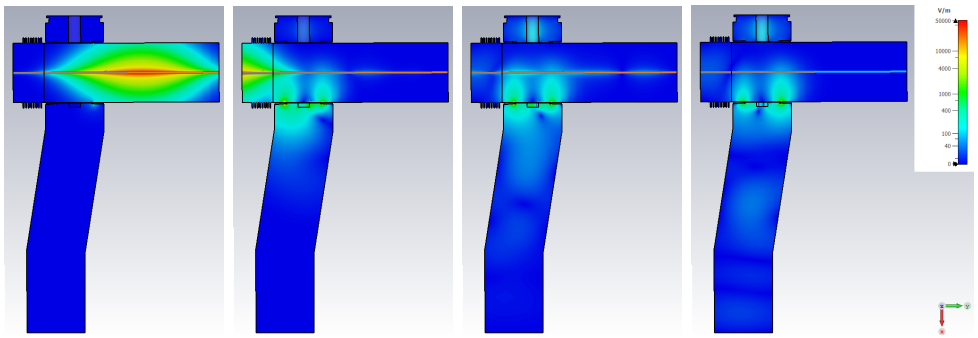

(c) Manifold with Shield 4, gap of 1mm

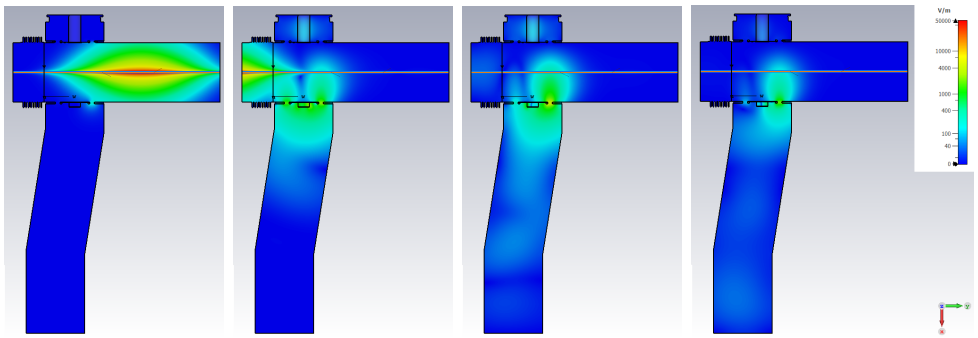

(d) Manifold with Shield 4, gap of 11mm

Figure 42: Comparison of the electric field in the different manifold configurations. From left to right the electric field correspond to the point in time of 2.5 ns, 3.8 ns, 5.1 ns and 9.95 ns respectively. The bunch of charged particles traverses the manifold from the right to the left. (continues)

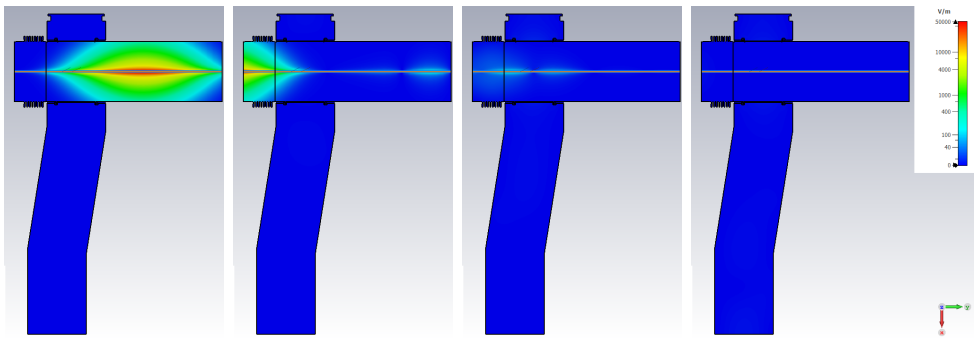

(e) Manifold with Shield 2

Figure 42: Comparison of the electric field in the different manifold configurations. From left to right the electric field correspond to the point in time of 2.5 ns, 3.8 ns, 5.1 ns and 9.95 ns respectively. The bunch of charged particles traverses the manifold from the right to the left.

This page is intentionally left blank.

4

THE CASE OF THE PS SPARE FAST EXTRACTION SEPTUM - SMH16

The fast extraction septum PE.SMH16.3 is one of two extraction septa which are used to deflect protons and ions for the extraction transfer line TT2 from SS16 [9] [8]. Figure 43 shows one of the SMH16.3 installed in the PS machine [1].

Figure 43: Picture of SMH16.3 in the PS machine, taken from the PS Ring webpage [1].

4.1 PROBLEM DESCRIPTION

Within the task of completing the impedance model of the PS, an impedance analysis of this existing machine element was required for determination of beam impedance contribution, however, only paper documentation of the septa is available. Due to the envisaged change of the PS layout which would lead to a replacement of the SMH16 [7] with an eddy current septa, a full modeling of this geometry for detailed EM-analysis and calculation of beam impedance was omitted. It was instead decided to determine the impedance contribution by measurement only. Hence, wire measurements have been carried out on the PE.SMH16.3 tank which shall provide sufficient information of the existing impedance contribution. As of today, two SMH-septa exist at CERN of which one is installed in the PS in the locations 16, whereas the other remains as a spare.

4.2 METHOD OF WIRE-MEASUREMENT

The coaxial wire method was used in order to evaluate the longitudinal impedance contribution of the SMH16.3. This method relies on the fact that the electromagnetic field distribution of an ultra-relativistic beam is very similar to that of a TEM line [10].

To perform the measurement, a thin (d=0.3 mm) stretched copper wire is placed in the beam position inside the device under test (DUT), this way forming a coaxial-like set-up. The wire is soldered at both ends to a series matching resistor attached to a type-N connector. This connection with the matching resistor and connector is made in a sucobox that is mounted to the flange cover on the outside of the DUT. Figure 44 shows a sketch of the setup to perform the wire measurement. The series matching resistor is needed to obtain a matching of the impedance Z_L of the TEM line to the characteristic impedance $Z_0 = 50\ \Omega$ of the measuring device (VNA) and its cables. Typically, the characteristic impedance formed by the wire and the DUT is considerably larger than 50 Ω and would create a large mismatch. The value of the matching resistors is obtained by the formula $R = Z_L - Z_0$ [3]. Z_L is the characteristic impedance of the thin wire inside of the magnet, and its approximate value can be calculated using the model of a wire between two parallel conducting plates $Z_L = 60ln\left[1.27\frac{D}{d}\right]$ [3], where D is the distance between plates and d is the diameter of the wire.

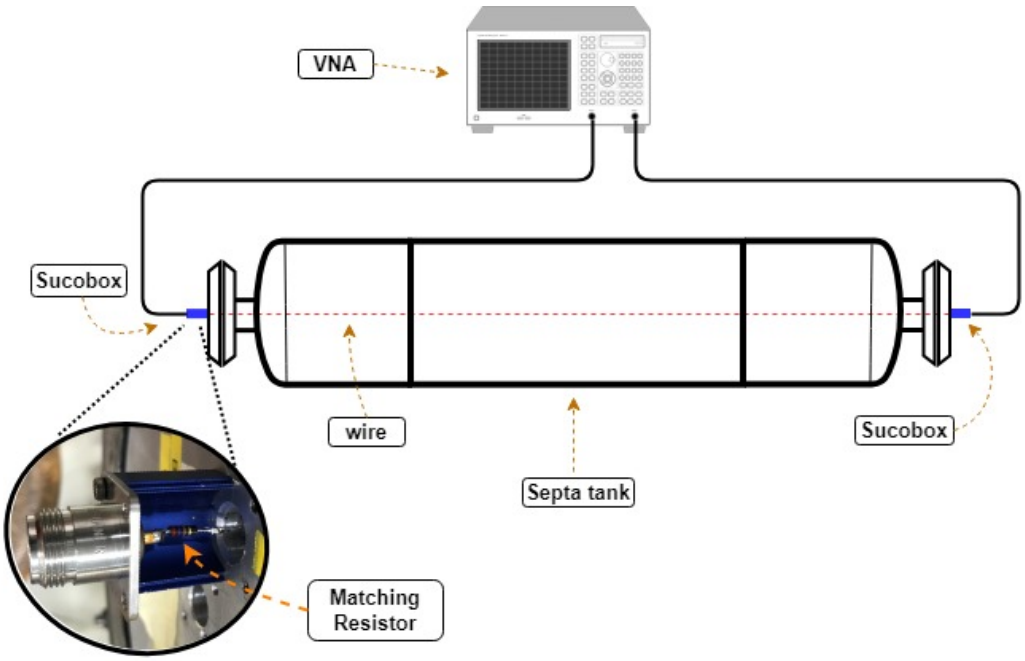

Figure 44: Wire measurement setup.

The SMH16.3 have a distance between the plates of $D = 70$ mm and a diameter of wire of $d = 0.3$ mm, which results in a matching resistor value of $R \approx 291.5\ \Omega$.

For the measurement, a resistor value of 280 Ω was used as a close approximation, however, since this is not a perfect matching, multiple resonances are still showing up on the signal. These were manually taken out by using a running average filter only on specific intervals of the measured signal. The motivation for this manipulation and raw data can be found in the section 4.5.

S-parameter measurements were carried out with a VNA and Figure 45 shows the measured transmission ($S_{21_{DUT}}$) for a frequency range of 1 MHz to 2 GHz.

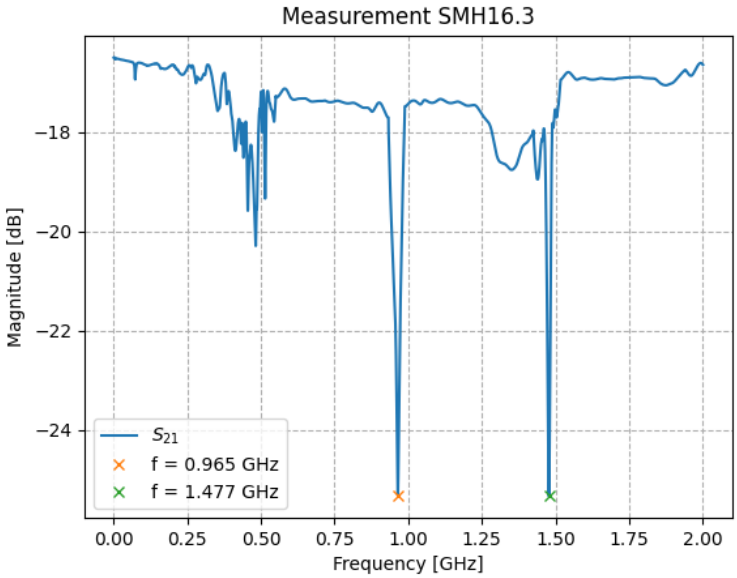

Figure 45: Measured $S_{21_{DUT}}$.

4.3 IMPEDANCE RESULTS

For the determination of the impedance [3], some corrections to amplitude and phase of the measured $S_{21_{DUT}}$ raw data need to be performed. For the $S_{21_{DUT}}$ amplitude, the attenuation caused by the resistors needs to be removed and the phase needs to be unwrapped. This corrected $S_{21_{DUT}}$ is normalized against the transmission of a reference line ($S_{21_{REF}}$). For practical reasons the $S_{21_{REF}}$ is considered the same as the one corresponding to an ideal matched line[3]. The log formula [10] was used to calculate longitudinal impedance and the result is shown in Figure 46.

It can be observed one smaller resonance at about 48 MHz and two larger resonance peaks at 965 MHz and 1.47 GHz, respectively, which were an indicator that the shielding might not be effective.

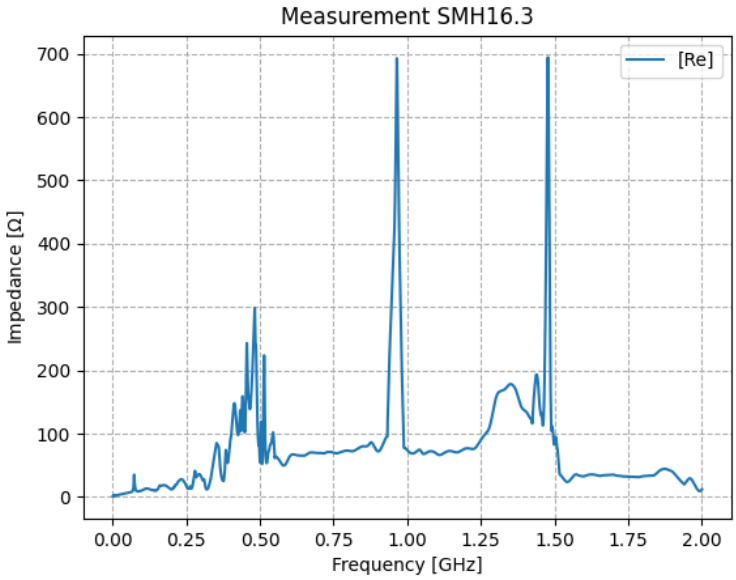

Figure 46: Calculated longitudinal impedance

4.4 DETECTION OF NON-CONTACTING RF FINGERS AND CORRECTIVE MEASURES

A cross-check of the shielding after the removal of the flange covers showed that many RF fingers were lifted and thus, not making proper contact. These RF fingers are supposed to provide contact between the internal RF shield and the flange on both ends of the outer tank. As can be seen on Figure 47 all RF fingers on the bottom side are lifted and in addition, some of them are twisted on the top side.

This problem occurred on both ends of the tank and could be traced as the cause of the resonant peaks observed in the measurement. After discussing this with the equipment owner, they proceeded to open the tank and repair the RF finger contacts.

The measurement was repeated after the repair was done and the results can be seen on figure 48, where the new measurement is compared to the one before the repair. This confirms that the poor contact caused by the bent RF fingers were in fact the cause of the resonances, now almost all of them were suppressed. The peaks around 1 GHz and 1.5 GHz are still present but greatly attenuated.

4.5 MOTIVATION FOR MEASUREMENT DATA MANIPULATION / MEASUREMENT RAW DATA

The matching between the VNA and the DUT at the flange interface is not perfect and, as a consequence, multiple reflections (that resemble a sinusoidal wave pattern)

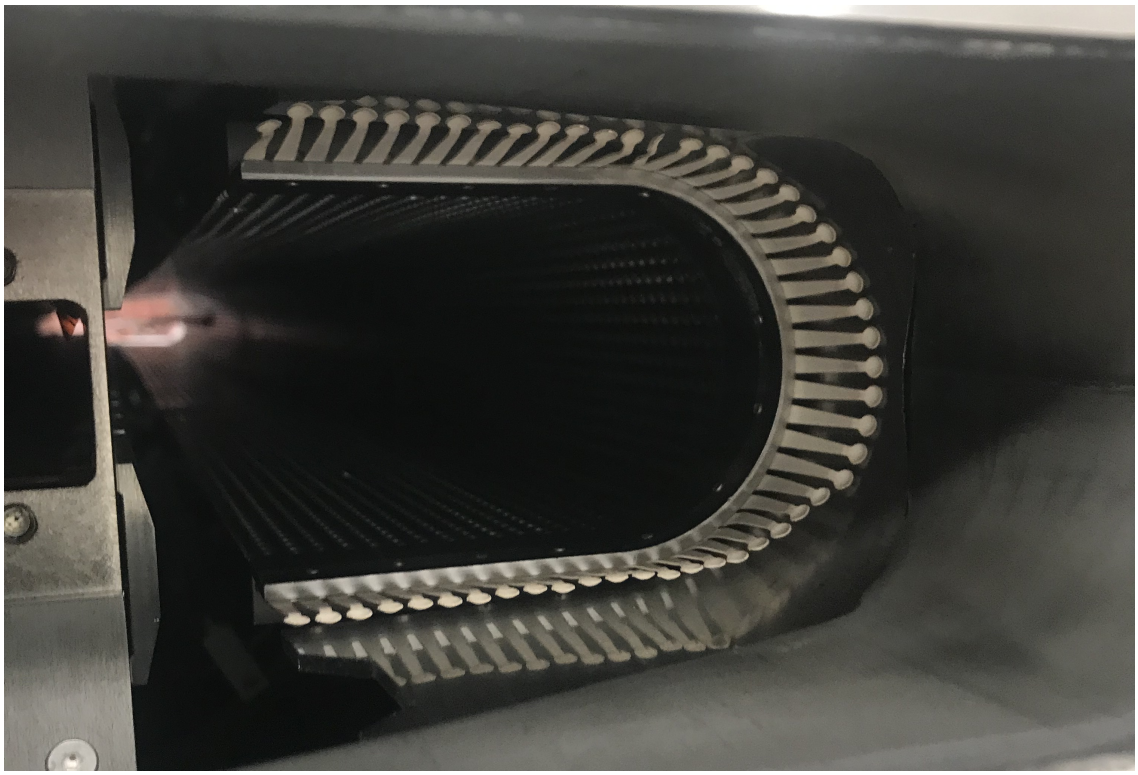

Figure 47: Non contacting RF fingers.

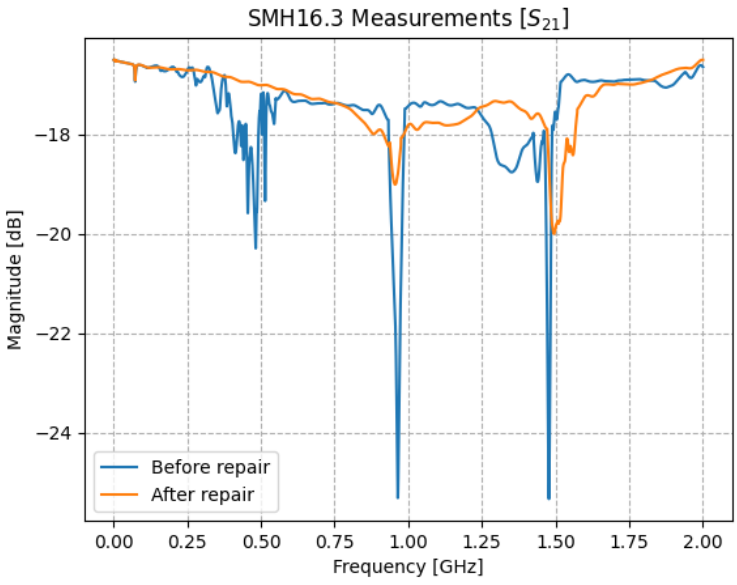

Figure 48: S_{21} measurements before and after Repair.

are observed as overlaying the measurement signal. The raw measurement data, before and after the repair, can be see in Figure 49 and Figure 50.

These mismatches would result in non-physical impedance values, for example give a negative real impedance. Hence the need to manipulate the raw data before computing the beam impedance. It was decided to perform a CST simulation of an ideal reference line, to confirm that this multiple reflections are really due to the

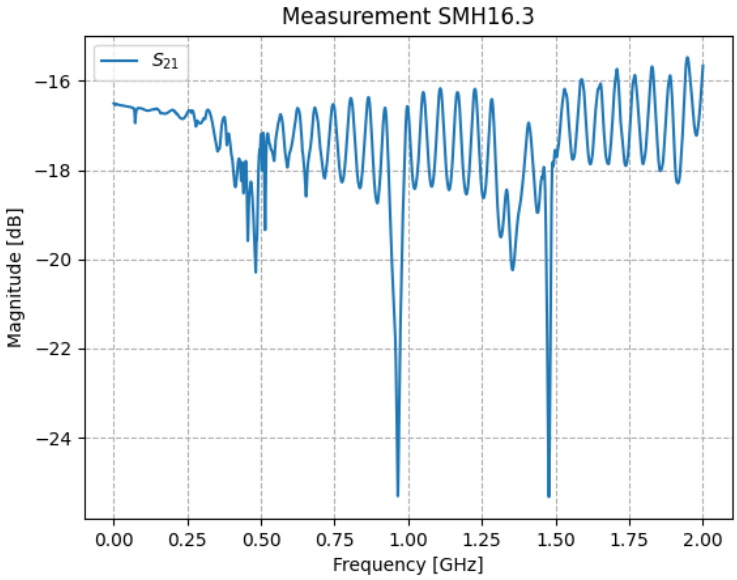

Figure 49: Raw data trace of S_{21} with non-contacting RF fingers (before repair) and overlaying resonance pattern due to line mismatch.

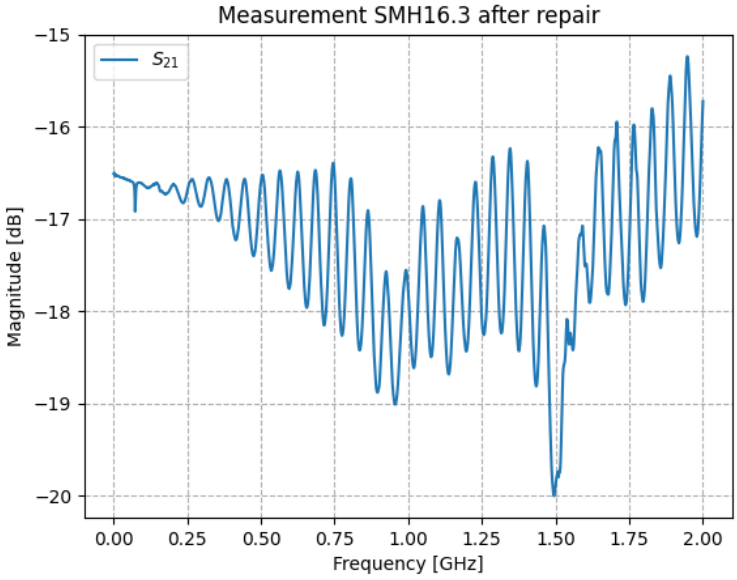

Figure 50: Raw data trace of S_{21} with re-worked RF fingers and overlaying resonance pattern due to line mismatch.

mismatches of the measurement setup. This CST model simulates the performed wire measurement(including coaxial connectors and suco boxes) of an ideal, closed, transmission line (Figure 51). The model has the same length and internal dimensions as the DUT that was measured. The simulated S_{21} of the ideal REF line can be seen in Figure 51d, this clearly shows the same multiple reflections. The Δ f between peaks has roughly the same value as the one in the measurement data, which confirms that these multiple resonances are due to the poor mismatch and the

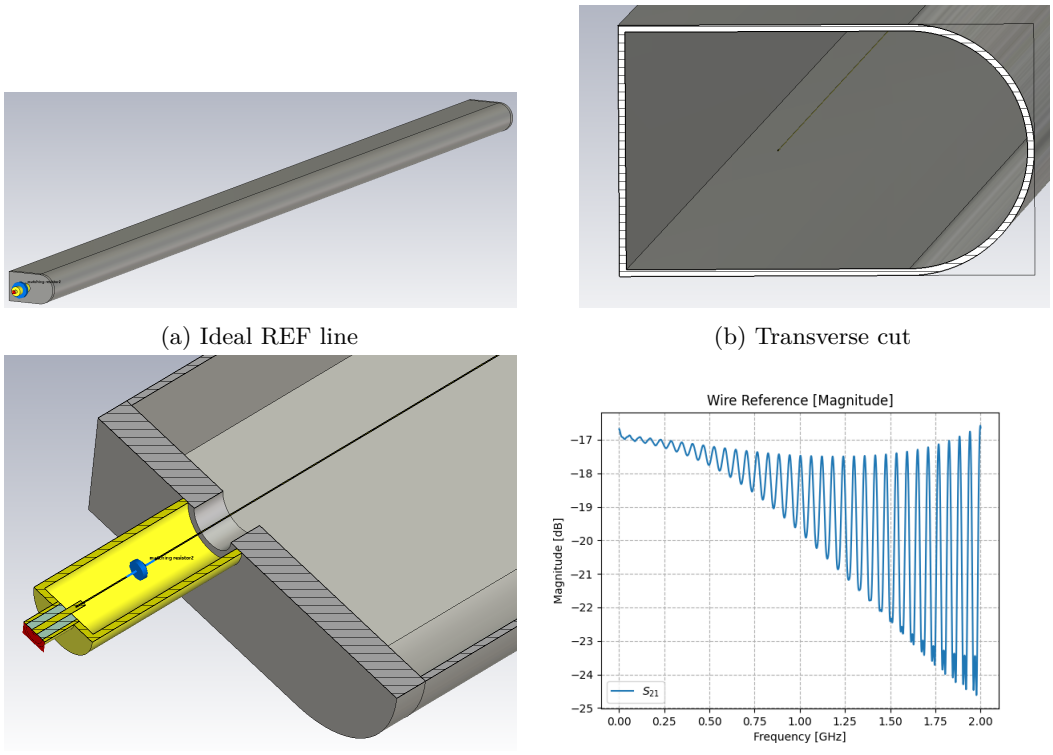

(a) Ideal REF line

(b) Transverse cut

(c) Longitudinal cut

(d) S_{21} of ideal REF line

Figure 51: CST Ideal reference line simulation

measurement setup, and are not true resonances caused by the geometry of the device.

In order to correct the measured signal and remove the multiple reflections it was decided to filter the raw data, but only in specific intervals, by using a running average filter. This intervals were chosen to be only on parts of the signal containing resonances that were considered to be due to the mismatch, for example, where the signal looks like a "clean" sinusoidal wave without an abrupt change in amplitude. The intervals chosen, and the respective filtered result can be seen in the plots of Figure 52.

Figure 53 and Figure 54 show the overlay of the original signal and its filtered version, for both measurements.

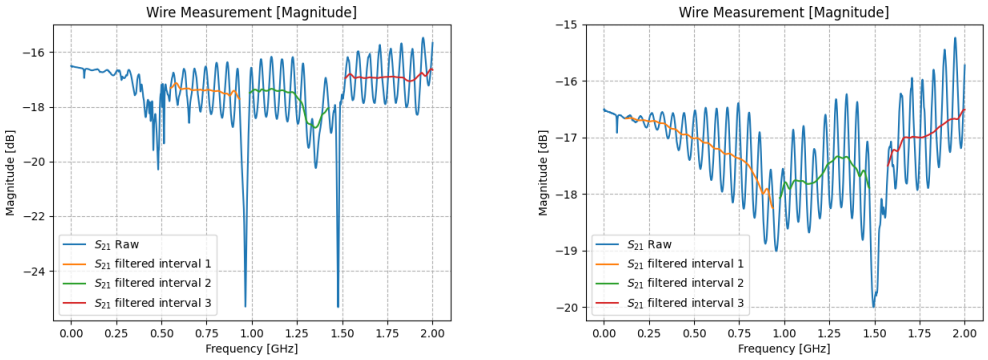

(a) S_{21} Before repair.

(b) S_{21} After repair.

Figure 52: S_{21} Filtered intervals of measured data.

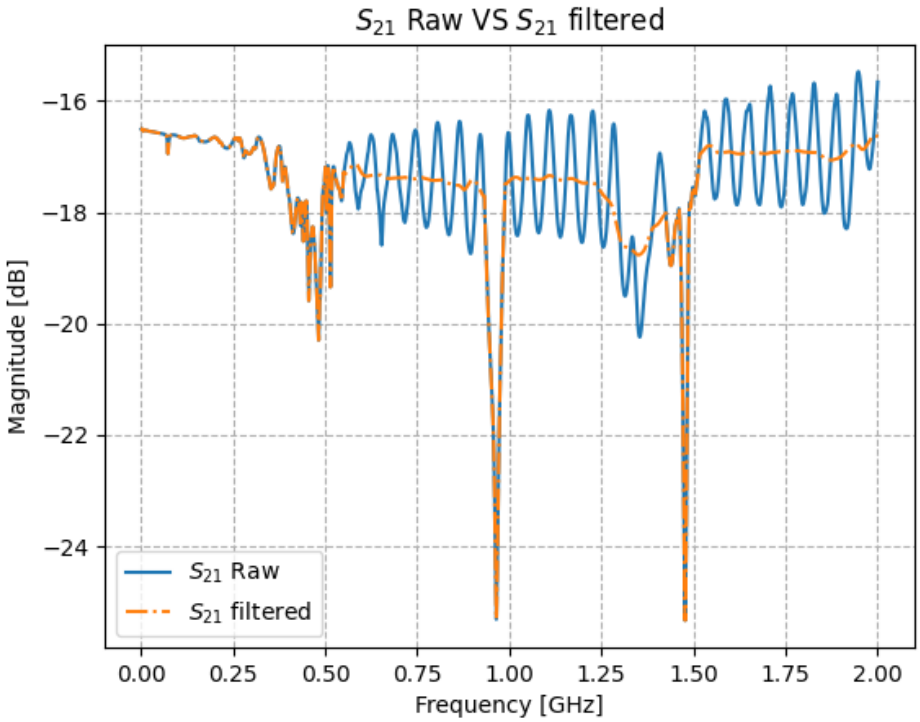

Figure 53: Comparison between RAW and filtered S_{21} (Before repair).

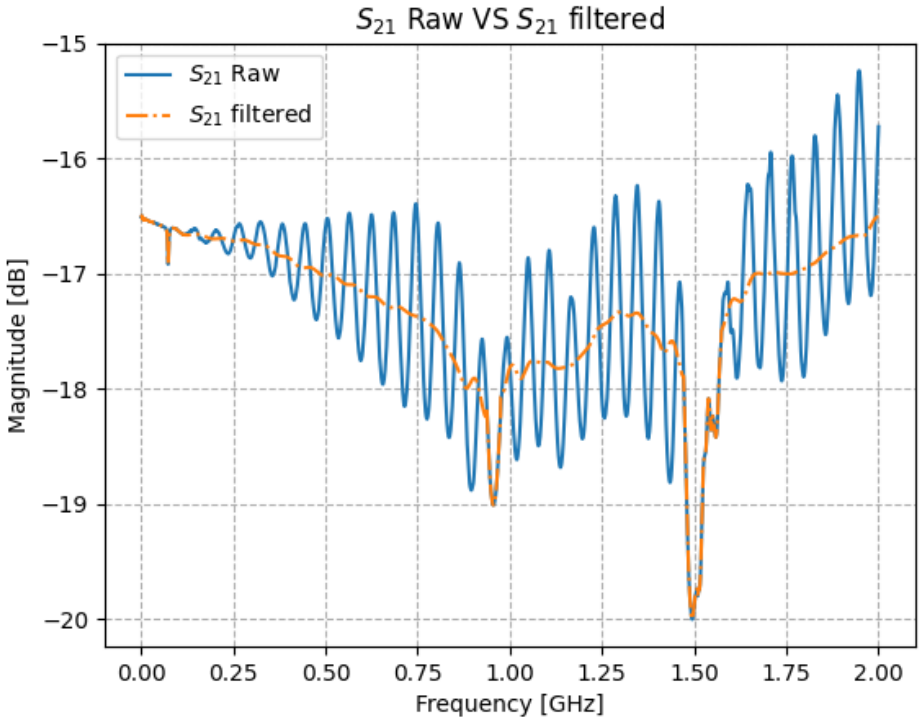

Figure 54: Comparison between RAW and filtered S_{21} (After repair).

This page is intentionally left blank.

5

CONCLUSION

The main goal of this internship was to design and test of RF shielding for beam impedance reduction in CERN accelerators. This work was focused on investigating the beam coupling impedance in the PS accelerator, more specifically in its pumping manifolds. Through a combination of simulations and measurements, the impedance contribution of the pumping manifold was thoroughly examined. A high beam coupling impedance on this manifolds led to the design and simulation of various shields to mitigate the impedance effects.

Several shield designs were proposed and evaluated, with Shield Design 2 being a strong candidate. This particular design demonstrated superior performance and simplicity in construction compared to Shield design 4, highlighting its potential for practical implementation. Shield design 2 and Shield design 4 were appreciated by the PS coordination team and approved for further validation, by performing RF measurements on a shield prototype, and subsequent installation in the empty manifolds of the accelerator.

Furthermore, after compliance impedance measurements in a SMH16 spare geometry it was identified a critical issue of defective RF shielding fingers. The defective shielding was corrected, but this raised concern about the shielding effectiveness of other parts, currently in use in the accelerator, with similar RF fingers. This work originated a measurement report publication at CERN, entitled *Measurement of the SMH16.3 Magnetic Septa* [13].

This page is intentionally left blank.

BIBLIOGRAPHY

[1] Jeroen Belleman and Simon Mataguez. *The PS Layout Database*. URL: http://psring.web.cern.ch/psring/pictures/big/ss16i-a.jpg.

[2] Amos Breskin and Rüdiger Voss. *The CERN Large Hadron Collider: Accelerator and Experiments*. Geneva: CERN, 2009. URL: http://cds.cern.ch/record/1244506.

[3] Fritz Caspers et al. *Impedance measurement of the SPS MKE kicker by means of the coaxial wire method*. 2000. URL: https://cds.cern.ch/record/960191.

[4] *CERN Beam Longitudinal Dynamics code BLonD*. http://blond.web.cern.ch. Accessed: 2022-11-09.

[5] *Computer Simulation Technology (CST) AG. Darmstadt, Germany*. :http://www.cst.com. Accessed: 2022-11-09.

[6] H Damerau et al. *LHC Injectors Upgrade, Technical Design Report*. 2014. DOI: 10.17181/CERN.7NHR.6HGC. URL: https://cds.cern.ch/record/1976692.

[7] Matthew Fraser. *Functional Specification for the Consolidation of PE.SMH16*. Geneva, 2022. URL: https://edms.cern.ch/document/2353265.

[8] Massimo Giovannozzi et al. *The CERN PS multi-turn extraction based on beam splittting in stable islands of transverse phase space: Design Report*. CERN, Geneva, 2006. DOI: 10.5170/CERN-2006-011. URL: https://cds.cern.ch/record/987493.

[9] Trygve Helseth et al. «FEASIBILITY STUDY FOR THE NOVEL CERN PS FAST EXTRACTION SEPTUM». In: *IPAC2021* (2021), pp. 2363–2366. DOI: 10.18429/JACoW-IPAC2021-TUPAB363. URL: https://cds.cern.ch/record/2812273.

[10] Thomas Kroyer and Fritz Caspers. «Longitudinal and transverse wire measurements for the evaluation of impedance reduction measures on the MKE extraction kickers». In: *CERN-AB-Note-2007-028* (2007).

[11] *PS RING MAGNET UNIT 080*. http://https://edms.cern.ch/document/224900/AE. Accessed: 2022-11-09.

[12] Wil Schilders. «Introduction to Model Order Reduction». In: vol. 13. Jan. 2008, pp. 3–32. ISBN: 978-3-540-78840-9. DOI: 10.1007/978-3-540-78841-6_1.

[13] Miguel Valente Dos Santos, Michela Neroni, and Christine Vollinger. «Measurement of the SMH16.3 Magnetic Septa». In: (2023). URL: https://cds.cern.ch/record/2870131.

[14] T.P. Wangler. *RF Linear Accelerators*. Physics textbook. Wiley, 2008. ISBN: 9783527623433. URL: https://books.google.fr/books?id=0JdgVI-UrikC.

[15] Bruno W Zotter and Semyon Kheifets. *Impedances and Wakes in High Energy Particle Accelerators*. WORLD SCIENTIFIC, 1998. DOI: 10.1142/3068. eprint: https://www.worldscientific.com/doi/pdf/10.1142/3068. URL: https://www.worldscientific.com/doi/abs/10.1142/3068.

DECLARAÇÃO

Declaro, sob compromisso de honra, que o trabalho apresentado nesta dissertação, com o título *"Design and test of RF shielding for beam impedance reduction in CERN accelerators"*, é original e foi realizado por Miguel Valente dos Santos (2182460) sob orientação de Telmo Rui Carvalhinho Cunha Fernandes (telmo.fernandes@ipleiria.pt).

Leiria, September of 2023

Assinado por: **Miguel Valente dos Santos**
Num. de Identificação: 14676310
Data: 2023.11.13 20:55:49+01'00'

Miguel Valente dos Santos